Department of Applied Physics

Ferromagnetic-Ferroelectric Domain Coupling in Multiferroic Heterostructures

Tuomas Lahtinen

Aalto University

DOCTORAL DISSERTATIONS

Aalto University publication series
DOCTORAL DISSERTATIONS 106/2013

Ferromagnetic-Ferroelectric Domain Coupling in Multiferroic Heterostructures

Tuomas Lahtinen

A doctoral dissertation completed for the degree of Doctor of Science (Technology) to be defended, with the permission of the Aalto University School of Science, at a public examination held at the lecture hall E of the Main Building on 27 June 2013 at 12.

Aalto University
School of Science
Department of Applied Physics
Nanomagnetism and Spintronics

Supervising professor
Prof. Sebastiaan van Dijken

Thesis advisor
Prof. Sebastiaan van Dijken

Preliminary examiners
Dos. Marina Tyunina, University of Oulu, Finland
Prof. Petriina Paturi, University of Turku, Finland

Opponent
Dr. Neil Mathur, University of Cambridge, United Kingdom

Aalto University publication series
DOCTORAL DISSERTATIONS 106/2013

ISBN 978-952-60-5230-4 (printed)
ISBN 978-952-60-5231-1 (pdf)
ISSN-L 1799-4934
ISSN 1799-4934 (printed)
ISSN 1799-4942 (pdf)
http://urn.fi/URN:ISBN:978-952-60-5231-1

Unigrafia Oy
Helsinki 2013

Finland

441 697
Printed matter

Aalto University

Abstract

Aalto University, P.O. Box 11000, FI-00076 Aalto www.aalto.fi

Author
Tuomas Lahtinen

Name of the doctoral dissertation
Ferromagnetic-Ferroelectric Domain Coupling in Multiferroic Heterostructures

Publisher School of Science

Unit Department of Applied Physics

Series Aalto University publication series DOCTORAL DISSERTATIONS 106/2013

Field of research Multiferroic heterostructures

Manuscript submitted 16 April 2013 **Date of the defence** 27 June 2013

Permission to publish granted (date) 17 May 2013 **Language** English

☐ **Monograph** ☒ **Article dissertation (summary + original articles)**

Abstract

In this thesis, strain-mediated coupling between magnetic films and ferroelectric $BaTiO_3$ substrates with regular ferroelastic domain structures is studied. Using optical polarization microscopy, it is shown that imprinting of ferroelectric domains into magnetic polycrystalline CoFe, amorphous CoFeB and crystalline Fe films can be achieved. The ferroelectric polarization and elongated *c*-axis of the $BaTiO_3$ substrates rotate by 90^o at ferroelectric domain boundaries. Transfer of this strain to the adjacent magnetic film induces local magnetoelastic anisotropy whose orientation and symmetry depends on the underlying ferroelectric domain. Furthermore, abrupt changes in the magnetoelastic anisotropy pin the magnetic domain walls onto the ferroelectric domain boundaries. As a result, the magnetic domain walls do not move in an applied magnetic field resulting in the formation of magnetically charged and uncharged domain walls at different field directions.

The strong coupling between magnetic and ferroelectric domains is used to demonstrate local magnetic switching and magnetic domain wall motion by purely electrical means. It is shown that a regular magnetic stripe pattern can be reversibly written and erased by the application of an electric field across the $BaTiO_3$ substrate. Moreover, the magnetic domain walls are dragged along by their ferroelectric counterpart in an external electric field. Both effects are explained by 90^o rotations of the ferroelectric polarization and the resulting strain-induced modification of the local magnetoelastic anisotropy. Similar strain-mediated effects, including local in-plane magnetization rotation by 90^o, are obtained when the multiferroic heterostructures are cooled or heated through the structural phase transitions of $BaTiO_3$.

Keywords ferromagnetic, ferroelectric, multiferroic, magnetism, magnetic domain, electric field control of magnetism, Barium Titanate

ISBN (printed) 978-952-60-5230-4 **ISBN (pdf)** 978-952-60-5231-1

ISSN-L 1799-4934 **ISSN (printed)** 1799-4934 **ISSN (pdf)** 1799-4942

Location of publisher Espoo **Location of printing** Espoo **Year** 2013

Pages 119 **urn** http://urn.fi/URN:ISBN:978-952-60-5231-1

Preface

Five years ago I started my Ph.D. studies in the new Nanomagnetism and Spintronics group (NanoSpin) at Aalto University as the first full-time group member. The topic of my research was electric field controlled magnetism, a relatively new and ambitious research field. During my time at NanoSpin, the laboratories have filled with new equipment, new members have joined the group and the group has established itself within the magnetic research community. The experiences I have gained during these years have been of utmost value. I am forever grateful to those, who have assisted and supported me during my academic career.

First and foremost, I would like to thank my supervisor, Prof. Sebastiaan van Dijken, for the countless hours he has invested in me. Without his guidance, knowledge, experience and intuition none of the work presented in this thesis would have been possible. It has been a pleasure working with Sebastiaan through these years.

I would also like to thank the successful collaborations that have been the backbone of this work. The magnetic modeling performed by Mr. Jussi Tuomi and Mr. Kévin Franke have played an integral role in the publications and I am grateful for their contributions. I would like to thank Dr. Qi Hang Qin and Mr. Witold Skowronski for helping me with cleanroom techniques and transport measurements. I would also like to thank Dr. Lide Yao, Dr. Yang-Jong Kim, Dr. Arianna Casiraghi, Dr. Sayani Majumdar, Mr. Mikko Kataja, Mr. Sampo Hämäläinen, Mr. Jukka Kärkimaa and especially Mrs. Laura Äkäslompo. I have been fortunate enough to work with these talented individuals of the NanoSpin group and I thank them for their support, assistance and insightful discussions.

Our group has enjoyed a close relationship with the Quantum Dynamics group. I would like to thank Dr. Francesco Massel, Dr. Jussi Kajala, Dr. Jami Kinnunen, Dr. Jani Martikainen, Dr. Dong-Hee Kim, Mr. Miikka Heikkinen

and Mr. Antti-Pekka Eskelinen for providing a social and enjoyable working environment.

I would also like to acknowledge the National Doctoral Programme in Materials Physics and Eemil Aaltosen säätiö for funding.

Finally, I dedicate this thesis to those closest to me, my family. I cannot express enough gratitude towards my parents, who have always supported me and my choices in life. Their contribution is immeasurable. I am most grateful to my girlfriend, Miss Marianne Jokinen, who has supported me throughout my Ph.D. studies and for her unconditional love and support. I am, truly, privileged to have her by my side.

Espoo, May 28, 2013,

Tuomas H. E. Lahtinen

Contents

List of Publications

This thesis consists of an overview and of the following publications which are referred to in the text by their Roman numerals.

I Tuomas H. E. Lahtinen, Jussi O. Tuomi, Sebastiaan van Dijken. Pattern Transfer and Electric-Field Induced Magnetic Domain Formation in Multiferroic Heterostructures. *Advanced Materials*, 23, 3187-3191, September 2011.

II Tuomas H. E. Lahtinen, Jussi O. Tuomi, Sebastiaan van Dijken. Electrical Writing of Magnetic Domain Patterns in Ferromagnetic/Ferroelectric Heterostructures. *IEEE Transactions on Magnetics*, 47, 3768-3771, October 2011.

III Tuomas H. E. Lahtinen, Kévin J. A. Franke, Sebastiaan van Dijken. Electric-Field Control of Magnetic Domain Wall Motion and Local Magnetization Reversal. *Scientific Reports*, 2, 258, February 2012.

IV Kévin J. A. Franke, Tuomas H. E. Lahtinen, Sebastiaan van Dijken. Field Tuning of Ferromagnetic Domain Walls on Elastically Coupled Ferroelectric Domain Boundaries. *Physical Review B*, 85, 094423, March 2012.

V Tuomas H. E. Lahtinen, Yasuhiro Shirahata, Lide Yao, Kévin J. A. Franke, Gorige Vemkataiah, Tomoyasu Taniyama, Sebastiaan van Dijken. Alternating Domains with Uniaxial and Biaxial Magnetic Anisotropy in Epitaxial Fe Films on $BaTiO_3$. *Applied Physics Letters*, 101, 262405, December 2012.

VI Tuomas H. E. Lahtinen, Sebastiaan van Dijken. Temperature Control of Local Magnetic Anisotropy in Multiferroic CoFe/$BaTiO_3$. *Applied Physics Let-*

ters, 102, 112406, March 2013.

Author's Contribution

Publication I: "Pattern Transfer and Electric-Field Induced Magnetic Domain Formation in Multiferroic Heterostructures"

The author designed the experiments, grew and characterized the samples by XRD and optical polarization microscopy, carried out the electric-field experiments, analyzed the data, discussed the results with co-authors and contributed to writing the manuscript.

Publication II: "Electrical Writing of Magnetic Domain Patterns in Ferromagnetic/Ferroelectric Heterostructures"

The author designed the experiments, grew and characterized the samples by XRD and optical polarization microscopy, analyzed the data, discussed the results with co-authors and contributed to writing the manuscript.

Publication III: "Electric-Field Control of Magnetic Domain Wall Motion and Local Magnetization Reversal"

The author designed the experiments, grew and characterized the samples by XRD and optical polarization microscopy, carried out the electric-field-control experiments, analyzed the data, discussed the results with co-authors and contributed to writing the manuscript.

Publication IV: "Field Tuning of Ferromagnetic Domain Walls on Elastically Coupled Ferroelectric Domain Boundaries"

The author designed the experiments, grew and characterized the samples by XRD and optical polarization microscopy.

Publication V: "Alternating Domains with Uniaxial and Biaxial Magnetic Anisotropy in Epitaxial Fe Films on $BaTiO_3$"

The author characterized the samples by optical polarization microscopy, analyzed the data, discussed the results with co-authors and contributed to writing the manuscript.

Publication VI: "Temperature Control of Local Magnetic Anisotropy in Multiferroic CoFe/$BaTiO_3$"

The author designed the experiments, grew and characterized the samples by XRD and optical polarization microscopy, carried out the temperature-controlled experiments, analyzed the data, discussed results with co-authors and wrote the manuscript with help from co-author.

1. Introduction

Magnetic materials are currently used for a wide range of practical applications including magnetic memory, and magnetic field sensors and actuators. The ability to control magnetism with an electric field has drawn wide research interest due to the potential it holds in lowering the power consumption of magnetic devices [1]. However, electric fields do not interact with magnetic materials. Multiferroic heterostructures are hybrid materials that combine both magnetic- and electric-field-sensitive ferroelectric materials. It has been shown that these materials exhibit a magnetic response in an electric field if the magnetic and ferroelectric materials couple.

One popular approach is to elastically couple magnetic thin films to ferroelectric substrates. Strain transfer from the ferroelectric substrate influences the properties of the magnetic film through inverse magnetostriction. In this work, microscopic aspects of this coupling mechanism are investigated in detail. In particular, correlations between the domain patterns of the ferroelectric substrates and magnetic films are imaged as a function of magnetic field, electric field and temperature.

This thesis starts with an introduction to ferromagnetism and magnetic materials with a focus on the energies that govern magnetic domain formation and the structure of magnetic domain walls (Chapter 2). A summary of ferroelectric $BaTiO_3$ including the ferroelectric domain structures and temperature related structural phase transitions follows (Chapter 3). Finally, Chapter 4 gives an overview of multiferroic materials and recent advances in electric field controlled magnetism in multiferroic systems.

The introductory Chapters are followed by an outline of the experimental methods, including thin film preparation methods and optical microscopy techniques (Chapter 5). The multiferroic heterostructures under study consist of ferroelectric $BaTiO_3$ substrates with magnetic CoFe, CoFeB and Fe films grown on top. Optical polarization microscopy measurements in conjunction with

a macrospin model and micromagnetic simulations are used to analyze the physics of these samples. An optical polarization microscopy technique is used for the first time to image ferroelectric and ferromagnetic domains simultaneously. This provides a platform to image domain evolution during magnetic and electric field controlled experiments.

Finally, Chapter 6 summarizes the main results of this thesis. Imprinting of ferroelectric domain patterns into magnetic films through interfacial strain transfer is demonstrated by imaging ferroelectric and magnetic domains and measuring local magnetic hysteresis curves. Subsequently, electric field and temperature controlled experiments indicate robust coupling of magnetic domains to their ferroelectric counterparts. As a key result, electric-field-induced magnetic domain control and magnetic domain wall motion in zero applied magnetic field are demonstrated.

2. Ferromagnetism

The characteristic feature of a ferromagnetic material is it's spontaneous magnetization, which is caused by alignment of atomic magnetic moments within the material. In ferromagnetic materials, the magnetic moment of the atoms originates in the electrons' spin, and their orbital motion around the nucleus. The spin-orbit interaction describes the coupling of the magnetic moments produced by the electron's spin with it's orbital motion around the nucleus.

A spin imbalance occurs in electron shells that are not full. The Pauli Exclusion Principle prevents electrons in the same quantum state from aligning their spins parallel. In many-electron electron shells the Coulomb force repels electrons that are in close proximity. To minimize the Coulomb energy, electrons align their spins parallel and fill the different quantum states first. This results in an unequal number of the two spin states giving the atom a net electron spin. Atoms with completely filled electron shells cannot be magnetic. In ferromagnetic 3-d transition metals such as Ni, Co and Fe the atomic magnetic moments primarily originate from the imbalance between the two spin states and the contribution of the orbital motion is relatively small [2].

The spontaneous magnetization of ferromagnetic materials originates from long-range ordering of atomic moments. Assuming localized electrons, the alignment of atomic moments can be described by the Heisenberg Hamiltonian

$$H = -\sum J_{ij} \mathbf{S_i} \cdot \mathbf{S_j}, \tag{2.1}$$

where J_{ij} is the exchange integral and $\mathbf{S_i}$, $\mathbf{S_j}$ are localized atomic spins. In ferromagnetic materials $J_{ij} > 0$ causing neighboring spins to align parallel. Due to the exchange interaction, atomic moments align below an ordering temperature T_c known as the Curie temperature. Above T_c, ferromagnetic ordering is overcome by thermal fluctuations [3].

The overall behavior of the magnetization in ferromagnetic materials is a competition between exchange, magnetostatic and anisotropy energies. Al-

though the exchange energy dominates at small length scales, magnetostatic and anisotropy energies influence long-range magnetic ordering [4]. This Chapter provides an overview of the different energy contributions in ferromagnetic systems and their influence on magnetic domain formation and the intrinsic properties of magnetic domain walls.

2.1 Exchange energy

Exchange energy dominates the alignment of atomic moments at small length scales, aligning atomic moments parallel in ferromagnetic systems. The direct exchange interaction that is present between atomic spins is described by Equation 2.1. The exchange interaction results in an exchange energy density ($\sim 0.1\,$eV/atom [5]), which can be expressed as [6]

$$E_{ex} = A(\nabla \mathbf{m})^2 \tag{2.2}$$

where $\mathbf{m} = \mathbf{M}/\mathrm{M_S}$ is the magnetization unit vector and A is the exchange stiffness constant.

2.2 Magnetostatic energy

Magnetostatic energy originates from free surface magnetic poles at an interface. In a uniformly magnetized sample stray fields are created outside the magnetic material and a demagnetizing field within the magnetic element. Although the magnetostatic energy is significantly smaller ($\sim$ 0.1meV/atom [5]) than the exchange energy it operates over longer length scales. The magnetic pole strength per unit surface area σ can be written as the component of magnetization perpendicular to an interface [7]

$$\sigma = \mathbf{M} \cdot \mathbf{n}, \tag{2.3}$$

where $\mathbf{n}$ is the unit vector normal to the interface. The magnetostatic energy density due to magnetic stray fields at the interface can be expressed as [8, 9]

$$E_{ms} = -\left(\frac{\mu_0}{2}\right)\mathbf{H}_\mathrm{d} \cdot \mathbf{M}, \tag{2.4}$$

where $\mathbf{H}_\mathrm{d}$ is the magnetic dipolar field created by the magnetization. This results in a demagnetizing field, which anti-aligns with the magnetization inside the magnetic sample. For an arbitrary shape the demagnetizing field is given

by

$$H_d = -NM, \tag{2.5}$$

where the demagnetizing tensor N is equal to unity for thin films with perpendicular magnetization.

2.3 Magnetic anisotropy

Magnetic anisotropy describes the angular dependence of magnetic energy. In a magnetic system containing anisotropy, the easy axes are defined as the magnetization orientation with minimum magnetic anisotropy energy and the hard axes are aligned along directions with maximum energy. A measure of the anisotropy strength is the anisotropy constant K_i, which is an energy density associated with an anisotropy contribution, i.

Magnetocrystalline and magnetoelastic contributions dominate the magnetic anisotropy landscape in the multiferroic systems studied in this thesis. The origins of these anisotropies are discussed in more detail below.

2.3.1 Magnetocrystalline anisotropy

Magnetocrystalline anisotropy arises from the symmetry of crystalline lattices and the elongated charge distribution around atoms due to the spin-orbit coupling. If we expand the free energy of a cubic magnetocrystalline system, E_c in terms of the directional cosines, m_1, m_2 and m_3, where $m_i = M_i/M_S$, we get [6]

$$E_c = K_1(m_1^2 m_2^2 + m_1^2 m_3^2 + m_2^2 m_3^2) + K_2(m_1^2 m_2^2 m_3^2)\ldots, \tag{2.6}$$

where K_1 and K_2 are first and second order anisotropy constants. In crude terms, the sign of K_1 determines whether $\langle 001 \rangle$ or $\langle 111 \rangle$ are the magnetocrystalline easy axes. As an example, Fe has magnetocrystalline easy axes along $\langle 001 \rangle$ ($K_1 > 0$), while in Ni the magnetocrystalline easy axes are along $\langle 111 \rangle$ ($K_1 < 0$) [10–13].

Amorphous ferromagnetic materials exhibit no magnetocrystalline anisotropy as no crystal symmetry is present. Similarly, completely randomly oriented polycrystalline materials will exhibit small magnetocrystalline anisotropy as the magnetocrystalline anisotropies of the individual grains cancel over macroscopic length scales.

2.3.2 Magnetoelastic anisotropy

Applying a mechanical strain to a ferromagnetic material induces a magnetoelastic anisotropy, otherwise known as the inverse magnetostriction effect [14, 15]. The strength of the magnetoelastic anisotropy is proportional to the stress σ and magnetostriction λ_s of the material. The magnetoelastic anisotropy constant K_{me} for *isotropic* materials can be written as [6]

$$K_{me} = -\frac{3\sigma\lambda_s}{2}, \tag{2.7}$$

where σ is proportional to the strain ε via Young's modulus Y. Isotropic systems include polycrystalline films with random texture and amorphous films [16]. Magnetoelastic anisotropy in amorphous systems originates from so-called bond-orientation anisotropy, where the anisotropy depends on average bond lengths [15,17–21]. Applying a tensile strain to an amorphous system increases the average bond length along the direction of strain leading to magnetoelastic anisotropy. The anisotropy energy of an isotropic system experiencing uniaxial strain can be written as

$$E_{me} = -K_{me}\sin^2\phi, \tag{2.8}$$

where ϕ is the angle between the magnetization and the strain axes. The magnetoelastic easy axis can either lie parallel or perpendicular to the direction of uniaxial strain. The sign of the magnetostriction λ_s of the material and the sign of the strain ε dictate the sign of K_{me}. As an example, if a film experiences uniaxial tensile strain ($\varepsilon > 0$) and has a positive magnetostriction then $K_{me} < 0$ leading to minima of E_{me} lying parallel to the direction of the tensile strain axis. If the same material were to experience a compressive strain ($\varepsilon < 0$) the magnetoelastic easy axis would lie perpendicular to the strain axis.

For crystalline systems the magnetoelastic anisotropy contribution depends on the direction of strain with respect to the crystalline axes. The general form of magnetoelastic energy in a crystalline system can be written as [22]

$$\begin{aligned} E_{me} = {} & B_1\left(\alpha_1^2\varepsilon_x + \alpha_2^2\varepsilon_y + \alpha_3^2\varepsilon_z\right) \\ & + B_2\left(\alpha_1\alpha_2\varepsilon_{xy} + \alpha_2\alpha_3\varepsilon_{yz} + \alpha_3\alpha_1\varepsilon_{zx}\right), \end{aligned} \tag{2.9}$$

where B_i are the magnetoelastic anisotropy constants, α_i are the directional cosines of the magnetization with respect to the crystalline axes, ε_i are normal strains along the crystalline axes and ε_{ij} are shear strains.

In epitaxial systems the magnetocrystalline anisotropy (Equation 2.6) and the magnetoelastic anisotropy (Equation 2.9) both contribute to the total anisotropy energy. For a crystalline material experiencing normal strain the magnetoelastic anisotropy dominates the magnetocrystalline anisotorpy above a critical strain value ε_c, which can be written as

$$\varepsilon_c = \frac{|K_1|}{|B_1|}. \tag{2.10}$$

For example, using bulk values for Fe ($K_1 = 4.8\times10^4 J/m^3, B_1 = -2.9\times10^6 J/m^3$ [6]) this gives $\varepsilon_c = 1.7\%$, i.e. above 1.7% lattice strain the magnetoelastic anisotropy becomes the dominant anisotropy contribution.

2.4 Zeeman energy

The Zeeman energy describes how the magnetization of a sample interacts with an external magnetic field. The Zeeman energy can be written as

$$E_z = -\mu_0 \int \mathbf{M}\cdot\mathbf{H}\,\mathrm{d}V, \tag{2.11}$$

where $\mathbf{H}$ is the external magentic field and $\mathbf{M}$ is the sample magnetization. For uniform magnetization and uniform external magnetic field this can be written as an energy density,

$$E_z = -\mu_0 M_s H\cos\left(\phi-\theta\right), \tag{2.12}$$

where $\left(\phi-\theta\right)$ is the angle between $\mathbf{M}$ and $\mathbf{H}$ and M_s is the saturation magnetization.

2.5 Magnetic domains and domain walls

The competition between the short-range exchange energy and long-range magnetostatic energy leads to magnetic domain formation [23]. Magnetic domains are areas of uniform magnetization separated by magnetic domain walls.

The exchange length indicates the length below which inter-atomic exchange interactions dominate and can be written as [24]

$$l_{ex} = \left(A/\mu_0 M_S^2\right)^{1/2}, \tag{2.13}$$

where A is the exchange stiffness and M_s is saturation magnetization. Magnetic domain formation is favorable when the size of a magnetic structure becomes larger than l_{ex}. Figure 2.1 (a) illustrates magnetic domain formation in

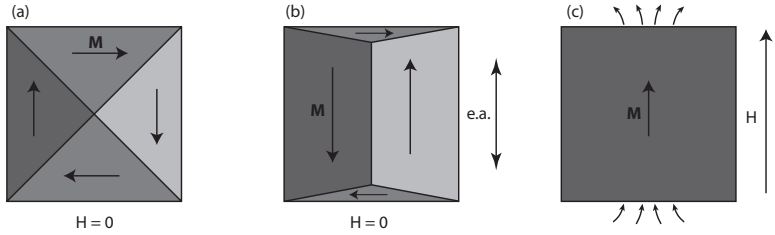

Figure 2.1. Schematic illustrations of different magnetization states, black arrows indicate direction of **M**. Magnetostatic stray fields are contained to within the sample in an isotropic system by the formation of domains, shown in (a). Domain formation in a uniaxial anisotropy system is shown in (b), where the easy axis is denoted by e.a. A mono-domain consisting of uniform magnetization along an external magnetic field H is shown in (c). Field lines indicate magnetostatic stray fields created at the surface. Adapted from [26].

an isotropic magnetic system with no applied external magnetic field. To minimize the magnetostatic, energy the magnetization aligns parallel to the sample edges. If a uniaxial anisotropy is present (i.e. magnetocrystalline or magnetoelastic), the majority of the magnetization will align along the uniaxial easy axis. To reduce the magnetostatic energy small 'closure' domains form with magnetization perpendicular to the magnetic easy axis near the bottom and top edges of the magnetic structure, as shown in Figure 2.1 (b). The energy penalty for having magnetization along the hard axis is compensated by a minimization of the magnetostatic energy.

If a magnetic sample is placed in an external magnetic field (H), the Zeeman energy E_z will force the magnetization to align with H above the saturation field. This creates a mono-domain state where the magnetization over the entire sample is uniform, as shown in Figure 2.1 (c). The total energy of magnetic domains can be written as the sum of the different energy contributions [25]:

$$E_{domain} = E_{ex} + E_{ms} + E_c + E_{me} + E_z. \tag{2.14}$$

The width of domain walls (δ_w) that separates magnetic domains is determined by a competition between the exchange energy and the magnetic anisotropy. Large exchange stiffness widens the domain walls as it minimizes the magnetization rotation between neighboring atomic spins. On the other hand, a large magnetic anisotropy decreases the domain wall width to minimize the energy penalty for having the magnetization pointing away from the magnetic easy axis inside the domain wall. In magnetic films, two types of domain walls can exist; the Bloch and Néel wall, shown schematically in Figure 2.2.

In a 180° Bloch wall the magnetization rotates out-of-plane in the wall. For

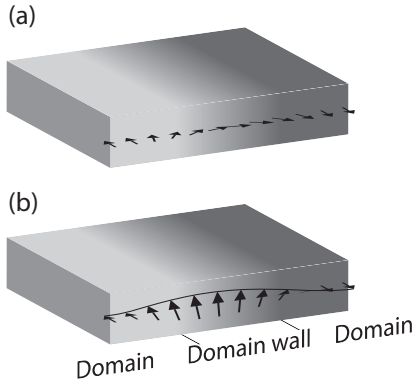

Figure 2.2. Illustration of (a) a Néel domain wall and (b) a Bloch domain wall in magnetic films.

180° Bloch walls the domain wall width can be written as [6]

$$\delta_B^{\parallel} = \pi \left(\frac{A}{K_u} \right)^{1/2}, \tag{2.15}$$

where A is the exchange stiffness and K_u is the uniaxial anisotropy constant. Bloch walls are energetically favorable for thick magnetic films.

In thin magnetic films with uniaxial anisotropy the magnetization rotates in the plane of the film. This results in 180°–Néel type domain walls, illustrated in Figure 2.2. Here, the magnetization points perpendicular to the domain wall in the center of the wall creating magnetostatic stray fields between the domains. The resulting magnetostatic energy increases linearly with film thickness in a Néel wall, therefore, Néel walls are limited to thin magnetic films. No simple formula exists for the Néel domain wall width as it depends not only on the exchange stiffness and magnetic anisotropy of the material but also on magnetostatic interactions within the domain wall. The width of a Néel wall can be determined by micromagnetic simulations. To determine the domain wall width from micromagnetic simulations the spin rotation across the wall is extracted. The following definition for domain wall width is used in this work:

$$\delta = \int \cos^2 \phi \, \mathrm{d}x, \tag{2.16}$$

where x lies perpendicular to the domain wall and ϕ is the spin rotation in the domain wall.

In non-180° Néel walls, the magnetization in the center of the wall can either point perpendicular or parallel to the domain wall. If the magnetization is perpendicular to the domain wall (satisfying $(\mathbf{M_1} - \mathbf{M_2}) \cdot \mathbf{n} = 0$, where $\mathbf{n}$ is a unit vector perpendicular to the wall), it results in a magnetically uncharged domain wall, as shown in Figure 2.3 (a). If the magnetization at the center points

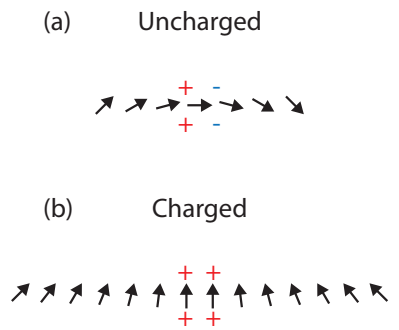

Figure 2.3. Uncharged Néel type domain wall (a) and charged domain wall (b).

along the domain wall, the magnetization in neighboring domains is aligned in a head-to-head or tail-to-tail configuration, which results in the accumulation of magnetic charges (Figure 2.3 (b)). The width of charged domain walls is about one order of magnitude wider than uncharged domain walls. In bulk magnetic samples the large magnetostatic energy associated with charged domain walls makes them unfavorable. However, in thin films their energy reduces with thickness, which makes their formation more favorable. In the multiferroic heterostructures under study in this thesis, pinning of magnetic domain walls on ferroelectric domain boundaries allows for the controlled formation of uncharged and charged domain walls by an appropriate selection of the magnetic field direction.

2.5.1 Magnetization reversal

The response of a magnetic film to an external magnetic field is characterized by a $M-H$ loop, shown in Figure 2.4. The $M-H$ loop indicates the projection of the magnetization vector onto the axis of the external magnetic field. In a magnetic system with uniaxial anisotropy the shape of the hysteresis curve depends on the angle of the magnetic field with respect to the easy anisotropy axis. The Stoner-Wohlfarth model can be used to describe magnetization behavior in a magnetic system with uniaxial anisotropy. The model assumes a mono-domain system with energy density

$$E = -K_u \cos^2(\phi) - \mu_0 H M_s \cos(\phi - \theta), \tag{2.17}$$

where ϕ is the angle between the magnetization and the easy anisotropy axis and θ is the angle between the external magnetic field and the easy anisotropy axis.

Two instances of the Stoner-Wohlfarth model are considered here; magneti-

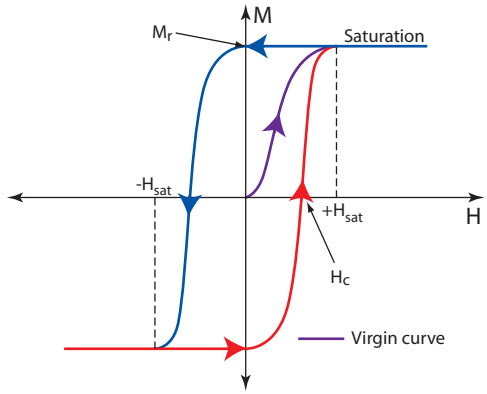

Figure 2.4. A schematic of a $M-H$ loop for a ferromagnetic material. M_r is the remanent magnetization and H_c is the coercive field. Magnetic saturation is achieve when $|H| > |H_{sat}|$.

zation reversal with the applied magnetic field along the easy anisotropy axis ($\theta = 0°$) and along the hard axis ($\theta = 90°$) of a magnetic material.

Easy axis. As the magnetization lies along the easy axis the anisotropy exerts no torque on the magnetization. In this case, the magnetization remains fixed until it rotates abruptly once the external magnetic field is reversed to a value of $H_s = K_u/2\mu_0 M_s$. This is schematically shown in Figure 2.5.

Hard axis. When measuring a hysteresis curve along a uniaxial hard axis ($\theta = 90°$) a competition between the anisotropy and Zeeman energy exists. At zero applied magnetic field the magnetization will align with the easy axis. Applying a magnetic field perpendicular to the easy axis increases the Zeeman energy and causes the magnetization to rotate away from the easy axis. Figure 2.5 shows the linear slope of a hysteresis curve measured along the hard axis. The magnetization continues to rotate (known as coherent rotation, illustrated in Figure 2.6) until it saturates at the saturation field $H_{sat} = K_u/2\mu_0 M_s$.

The slope of the hard axis hysteresis curve can be used to determine the uniaxial anisotropy strength. The energy minima of Equation 2.17 are first determined by derivation with respect to ϕ:

$$\frac{\mathrm{d}E_u}{\mathrm{d}\phi} = 2K_u \sin(\phi)\cos(\phi) + \mu_0 M_s H \sin(\phi - \theta) = 0. \tag{2.18}$$

As we are dealing with a hard axis measurement we can set $\theta = 90°$. After rearranging, this gives

$$K_u = \frac{\mu_0 M_s H}{2\sin(\phi)}. \tag{2.19}$$

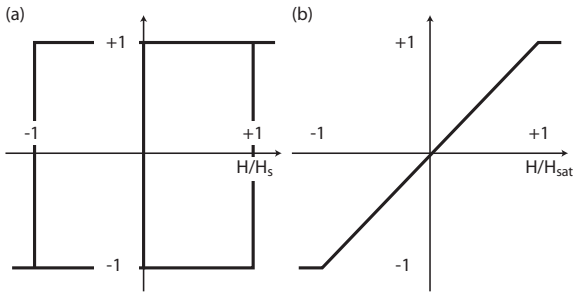

Figure 2.5. Schematics of hysteresis curves extracted from the Stoner-Wohlfarth model for a system with uniaxial anisotropy. (a) Shows an easy axis hysteresis curve and (b) and hard axis hysteresis curve.

The slope β around $H = 0$ of a hard axis hysteresis measurement with a normalized y-axis can be written $\beta = \sin(\phi)/\mu_0 H$, using units of Tesla for H. Substituting β gives

$$K_{me} = \frac{M_s}{2\beta}, \tag{2.20}$$

where M_s is the saturation magnetization of the magnetic film.

In uniform 2-D thin films, magnetization reversal mostly occurs through inverse domain nucleation and subsequent domain wall motion, as schematically shown in 2.6 (b). If the dimensions of a magnetic film are sufficiently large ($\gg \delta_{dw}$), small inhomogeneities in the energy landscape can cause spontaneous domain nucleation during magnetization reversal. The energy required to move a domain wall is often smaller than the domain nucleation energy and therefore the nucleated domain expands by lateral domain wall motion. Domain wall motion is hampered by pinning sites include grain boundaries, surface roughness and precipitates etc. [27–29]. The multiferroic heterostructures in this thesis are characterized by strong magnetic domain wall pinning on ferroelectric domain boundaries due to abrupt lateral modulations in the magnetic anisotropy. As a result, the magnetization mostly reverses by coherent rotation within the domains, which can be described by the Stoner–Wohlfarth model.

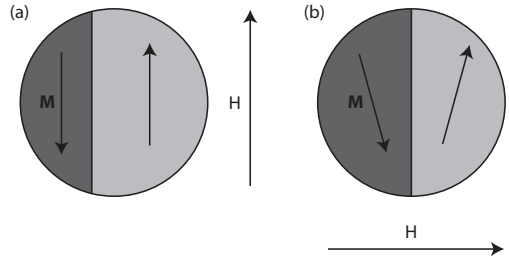

Figure 2.6. Magnetization reversal in thin magnetic films can either proceed by (a) coherent rotation or (b) lateral domain wall motion.

3. Ferroelectricity

Ferroelectric materials exhibit a spontaneous electric polarization, which can be switched using an external electric field. This is analogous to the magnetization and magnetization reversal in an applied magnetic field, which occur in ferromagnetic materials. Unlike ferromagnetism, ferroelectricity is connected to the structural properties of a material and not an intrinsic property of an atom. The mechanisms that give rise to ferroelectricity are order-disorder (e.g. KH_2PO_4) [30] and displacements of ions (e.g $BaTiO_3$) [31, 32]. A ferroelectric material is characterized by a hysteresis loop, called a $P-E$ loop. Similar to the $M-H$ loop of a ferromagnet shown in Figure 2.4, in a $P-E$ loop the polarization **P** replaces **M** and an external electric field **E** replaces **H**. The electric polarization **P** can be reversed by a sufficiently large external electric field E_c. Ferroelectric materials loose their spontaneous polarization and become paraelectric above a critical Curie temperature, T_c.

All ferroelectric materials also exhibit pyroelectricity, piezoelectricity and sometimes ferroelasticity. Pyroelectricity is a change in the polarization due to a change in temperature, ferroelasticity is the presence of a spontaneous strain, and piezoelectricity is the accumulation of charges due to an applied strain on the material. The polarization of a piezoelectric material can be written as [33]

$$P = Zd + E\chi, \tag{3.1}$$

where Z is the stress, d is the piezoelectric constant, E is the electric field and χ is the dielectric susceptibility.

The ferroelectric material used throughout this thesis is Barium Titanate, which will be discussed in more detail in the following Sections.

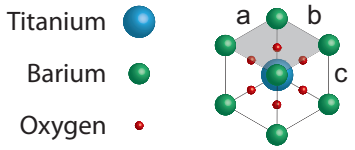

Figure 3.1. Perovskite structure of Barium Titanate.

3.1 Barium Titanate

Barium Titanate ($BaTiO_3$) is a perovskite structured material, which is ferroelectric, ferroelastic, piezoelectric and pyroelectric. The perovskite structure is shown schematically in Figure 3.1, where a Ti^{4+} ion is at the center of the unit cell, Ba^{2+} ions occupy the corners and O^{2-} ions are at the centers of the unit cell faces. At room temperature, $BaTiO_3$ is ferroelectric exhibiting a spontaneous polarization of 26 μC cm^{-2} [34]. The structural properties of Barium Titanate will be discussed in the following Sections with an emphasis on the structural phase changes associated with temperature and ferroelectric domain patterns at room temperature.

3.1.1 Structure

Below its Curie temperature of 393 K, $BaTiO_3$ is ferroelectric, exhibiting a tetragonal structure at room temperature (Figure 3.2). In the tetragonal phase, the polarization points along the $\langle 001 \rangle$ direction, aligning with the elongated c–axis of the tetragonal $BaTiO_3$ lattice (c/a = 1.1%). The electric dipole moment of the tetragonal $BaTiO_3$ unit cell is caused by a slight displacements of the O^{2-} ions with respect to the Ba^{2+} and Ti^{4+} ions. The displacements are illustrated in the top-view of the tetragonal phase in Figure 3.2, where the Ti^{4+} ion is shifted in the negative y-direction and the O^{2-} ions are shifted in the positive y-direction. The small displacements of the ions cause a net electric dipole, which in turn produces the spontaneous polarization in $BaTiO_3$.

Above its Curie temperature, $BaTiO_3$ is cubic and paraelectric, exhibiting no spontaneous polarization. When cooling through the Curie temperature, $BaTiO_3$ gains an elongation along the c–axis whilst the a– and b–axes of the unit cell slightly contract. This is a gradual process, which occurs over ~ 90 K. At 300 K the lattice elongation of $BaTiO_3$ amounts to 1.1% [35].

At 278 K, $BaTiO_3$ undergoes a second phase transition from tetragonal to orthorhombic. As a results of this phase transition the ferroelectric polarization rotates from $\langle 001 \rangle$ to $\langle 011 \rangle$ [36]. In the top-view of the orthorhombic phase,

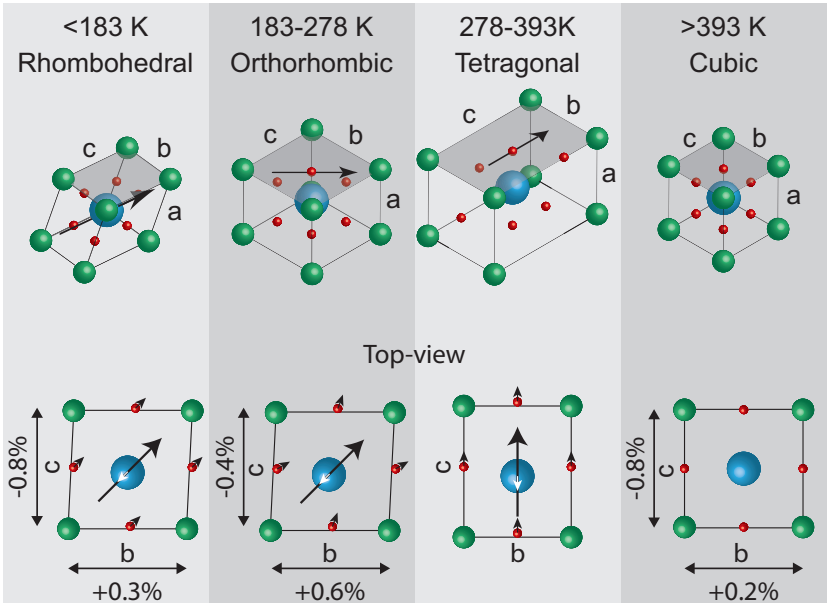

Figure 3.2. The unit cells for the four phases of $BaTiO_3$. Below are top-views of all of the phases showing ion displacements (small arrows) and the direction of **P**. Small arrows indicate direction of ion displacement. In the cubic phase (400 K) $a = b = c = 4.001$ Å, tetragonal phase (300 K) $c = 4.035$ Å, $a = b = 3.991$ Å, orthorhombic phase (250 K) $a = b = 4.018$ Å, $c = 3.987$ Å and rhombohedral phase (170 K) $a = b = c = 4.004$ Å. Lattice changes along the *b*– and *c*–axes with respect to the tetragonal phase are indicated as percentages in the top-view of the rhombohedral, orthorhombic and cubic phases.

shown in Figure 3.2, the O^{2-} ions are displaced in the direction of the polarization and are also slightly displaced towards the nearest Ti^{4+} ion [37]. The Ti^{4+} is displaced anti-parallel to the polarization and the Ba^{2+} ions continue to occupy the corners of the unit cell. The unit cell is slightly elongated in the direction of the polarization ($\alpha, \beta \neq 90°$).

The final phase transition from orthorhombic to rhombohedral occurs at 183 K. At this phase transition the polarization rotates from ⟨110⟩ to ⟨111⟩ ($a = b = c = 4.004$ Å) with $\alpha \neq 90°$. The O^{2-} ions are displaced in the direction of the polarization and Ti^{4+} ion is displaced anti-parallel.

3.1.2 Domains

Two types of domain patterns can exist in tetragonal $BaTiO_3$ (001) substrates; ferroelectric 180°– and ferroelastic 90°– domains. In ferroelectric 180° domain patterns, the polarization is out-of-plane (Figure 3.3 (a)). These domains are often referred to as *c*–domains. The existence of *c*–domains is unexpected in ferroelectric films and substrates as electric charges can accumulate at the surface. This would diminish the dipolar fields that drive the formation of *c*–

domains. However, rapidly cooling through the Curie temperature does not allow for sufficient charge build-up to compensate the dipolar fields generated by the spontaneous polarization [38].

A 90° rotation of the polarization results in a large ferroelastic strain at the domain boundary due to a lattice mismatch. In thin films, 90° domains form if $BaTiO_3$ is under uniaxial or biaxial tensile strain [39]. $BaTiO_3$ films can relax in-plane biaxial tensile strain by the formation of in-plane 90° domains with equal areas of a_1 and a_2 domains. Similarly, formation of a_1–a_2 domains in bulk $BaTiO_3$ is governed by the presence of pressure or an electric fields during preparation. The polarization in a_1–a_2 domains points head-to-tail in neighboring domains to reduce charging at domain boundaries. Ferroelectric domain boundaries lie at an angle of 45° with respect to the polarization direction, as shown in Figure 3.3 (b).

Alternatively, 90° a–c domains can also form in $BaTiO_3$ (001) substrates. In this domain structure the polarization alternates between in-plane and out-of-plane, as shown in Figure 3.3 (c). As the out-of-plane lattice parameters of the a– and c–domains are not equal a $\sim 0.5°$ inclination of the surface occurs at the domain boundary, shown in the inset of Figure 3.3 (c). The polarization points head-to-tail to minimize charging at the domain boundaries between a– and c–domains.

Ferroelectric and ferroelastic domains in $BaTiO_3$ have different ferroelectric domain wall widths (Figure 3.3 (d-f)). Ferroelectric c-domains are separated by a very narrow region where the polarization rotates over a few unit cells [40–42]. Ferroelastic domain boundaries are wider due to the lattice mismatch at the boundary and ferroelastic interactions. Typically the polarization rotates within 2 – 5 nm at the domain boundary [43–45]. Top-views of ferroelastic a_1–a_2 domains and a–c domains are shown in Figure 3.3 (e) & (f).

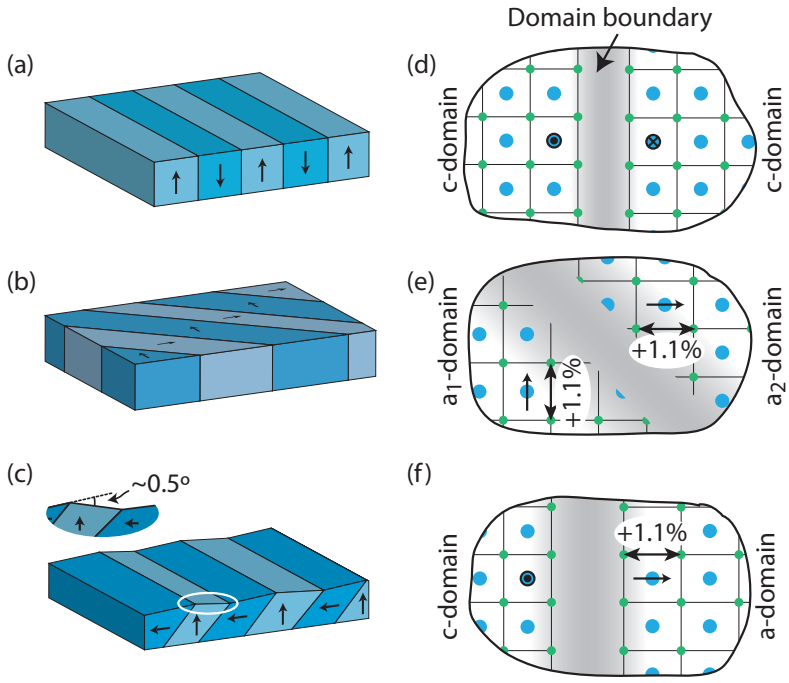

Figure 3.3. Domain patterns found in $BaTiO_3$ (001): c–domains are shown in (a), a_1–a_2 domains in (b) and a–c domains in (c) with an inset showing angle between domains at the surface. The structural changes at ferroelectric/ferroelastic domain boundaries are illustrated in (d)–(f).

4. Multiferroics

Multiferroic materials exhibit more than one ferroic order parameter (magnetic, electric aor elastic). Coupling between different ferroic order parameters holds potential for electric field controlled magnetic memory, 4-state logic and magnetoelectric sensors. This has contributed to an increased research interest in multiferroic materials in recent years [46–52].

Multiferroics exist in two forms; single-phase multiferroics and multiferroic heterostructures. Single-phase multiferroics intrinsically exhibit more than one ferroic order parameter. Typically either one or both of the order parameters are weak and only arise at low temperatures. Multiferroic heterostructures are artificially created by coupling two ferroic materials through an interface.

A brief discussion of the different multiferroic systems with an emphasis on electric-field-control of magnetism is presented here.

4.1 Single-phase multiferroics

Two categories of single-phase multiferroics exist; type I (ferroelectric and magnetic orders originate from independent phenomena) and type II (ferroelectricity is directly linked to the magnetic order). Type I multiferroics (e.g. $YMnO_3$) seldom have both magnetic and ferroelectric ordering temperatures above room temperature. The ordering temperatures for ferroelectricity and magnetism are different as the ferroelectric and magnetic moments arise from different phenomenon. This also leads to weak coupling between the ferroic states. The magnetic order originates from an imbalance between electron spin states and spin-orbit coupling. Ferroelectricity can occur due to lone pairs (ordering of polarizable 6*s* electron pairs), charge ordering (in equivalence of ion sites and bonds) or ion displacements.

$BiFeO_3$ is a commonly studied Type I single phase multiferroic. It is both antiferromagnetic and ferroelectric and it has been shown that the Curie tem-

perature of both the ferroelectric and anti-ferromagnetic phases are above room temperature [53]. Whilst $BiFeO_3$ has a large ferroelectric polarization of 90 μC cm^{-2} [53, 54], it is generally accepted that $BiFeO_3$ exhibits a weak magnetic moment of 0.05 μ_B/Fe [55–57]. Zhao *et al* demonstrated electric-field-control of antiferromagnetic domains in $BiFeO_3$ through coupling of antiferromagnetic and ferroelectric domains to the underlying ferroelastic domain structure [58].

In type II multiferroics (e.g. $TbMnO_3$, Ca_3CoMnO_6) the ferroelectric polarization directly originates from particular types of magnetic spiral or collinear magnetic structures. In both cases, magnetic interactions give rise to a net polarization at low temperatures, which directly couples the ferroic order parameters [59, 60]. The coupling between the ferroic order parameters has been largely limited to magnetic field control of ferroelectric polarization [61].

4.2 Multiferroic heterostructures

Using heterostructures to create artificial multiferroics allows for materials to be chosen for specific purposes requiring strong coupling, high ordering temperatures or large ferroic order parameters [51, 52]. In addition to the wide choice of ferroelectric and magnetic materials available, multiferroic heterostructures can also be tweaked by modifying the crystal orientation, lattice strain, electronic state, domain pattern and defect structure at the interface between the ferroic materials.

One method of coupling ferroic orders in multiferroic heterostructures is through nanopillar structures. Magnetic nanopillars in a ferroelectric medium are typically produced by self-assembly during co-deposition of magnetic and ferroelectric materials. This has been realized experimentally by co-deposition of ferroelectric perovskites ($BaTiO_3$, $PbTiO_3$) and magnetic spinels ($CoFe_2O_4$, $NiFe_2O_4$, and Fe_3O_4) [62–71] at high temperatures. The magnetic materials organize into crystalline pillars during deposition. An advantage here is the large contact surface area between the ferroelectric and magnetic materials and reduced mechanical clamping by the substrate [48]. Zavaliche *et al* demonstrated electric-field-induced magnetization switching in $CoFe_2O_4$ nanopillars in a $BiFeO_3$ medium [64]. As nanopillar structures heavily depend on self-assembly they are limited by the choice of materials leading to a restricted design and control of such structures.

Alternatively, the fabrication of thin film multiferroic heterostructures does not depend on self-assembly, therefore a larger variety of materials are available. Also, thin film heterostructures are appealing because the layered geom-

etry closely mimics the architecture of most practical devices. Three different mechanisms can drive electric-field-induced changes, namely charge modulation, exchange interaction and strain transfer.

4.2.1 Charge modulation

The electric field generated by a spontaneous polarization at the interface between a ferroelectric and thin magnetic film can modify the magnetization of the magnetic material. Screening of interface charges by depletion or accumulation of charge carriers at the interface affects the magnetic moment, anisotropy or magnetic ordering state. These effects have been demonstrated in metallic ferromagnets, magnetic oxides and dilute magnetic semiconductors [72–84]. Alternatively, atom displacements at the interface can affect the overlap between atomic orbitals altering the magnetic properties. For example, magnetic moment alterations have been demonstrate through *ab initio* calculations at a Fe/$BaTiO_3$ interface [72]. Here, the hybridization of Fe and Ti *3d*-orbitals cause a charge redistribution of majority and minority spins depending on the Fe–Ti bond length. Hence, electric-field-control of magnetization can be realized at a TiO_2 terminated $BaTiO_3$/Fe interface, since the Fe–Ti bond length depends on the polarization direction of the $BaTiO_3$. Similar effects have been calculated for $Co_2MnSi/BaTiO_3$ [85] and $Fe_3O_4/BaTiO_3$ interfaces [75]. Hybridization effects, which are strictly limited to the magnetic-ferroelectric interface have also been experimentally measured in tunnel junctions with a ferroelectric barrier [86–88].

4.2.2 Exchange interaction

Exchange interactions can couple single phase multiferroics that are both ferroelectric and antiferromagnetic (e.g. $YMnO_3$, $LuMnO_3$, $BiFeO_3$) to an adjacent magnetic film [89–97]. Coupling of magnetic domains to ferroelectric domains in CoFe/$BiFeO_3$ heterostructures has been demonstrated [91, 94, 97]. In these heterostructures, an easy magnetic anisotropy axis was created in the CoFe film parallel to the canted magnetic moment in the $BiFeO_3$. Since the magnetic moment in $BiFeO_3$ is directly linked to the ferroelectric polarization a correlation between magnetic and ferroelectric domains could be obtained. Furthermore, ferroelectric domains could be rewritten by applying an electric field, which resulted in the rearrangement of the magnetic domains.

4.2.3 Strain transfer

Electric field control of magnetization in multiferroic heterostructures can also be realized by elastical coupling between a magnetic thin film and a ferroelectric or piezoelectric substrate. Here, the lattice strain of the ferroelectric/piezoelectric is modified with an electric field. Through interfacial strain transfer this leads to a controllable strain in the adjacent magnetic film. Electric field control of the magnetoelastic anisotropy in the magnetic film is then obtained via inverse magnetostriction. The behavior of strain-controlled heterostructures depends on the competition between magnetoelastic and magnetocrystalline anisotropies, and magnetostatic and exchange interactions.

The nature of strain transfer from a piezoelectric or ferroelectric material are different. Piezoelectric materials produce a linear strain response in an applied electric field, which leads to a linear magnetic response [51, 98]. Due to the linear and reversible evolution of strain, the original strain state is restored when the electric field is removed. Therefore, piezostrain-induced magnetic changes are mostly volatile.

The electric-field-induced strain in a piezoelectric material can be either uniaxial or biaxial depending on the crystal orientation. $(1-x)$ $Pb(Zn_{1/3}Nb_{2/3})O_3-$ x $PbTiO_3$ (PZN-PT) and $(1-x)$ $Pb(Mn_{1/3}Nb_{2/3})O_3$ $-xPbTiO_3$ (PMN-PT) are common relaxor ferroelectric that exhibits a butterfly shaped piezostrain curve. The crystallographic orientation of these substrates can be used to select the type of strain it provides: (001) oriented crystals provide a biaxial in-plane strain response whereas (011) oriented substrates provide an uniaxial strain response in an out-of-plane electric field. PMN-PT has been utilized in tuning the magnetic properties of manganite [98–101], ferrite [102–106], and metallic magnetic films [107–109], and also in altering the electrical resistance of magnetic oxides [99, 101, 105, 110–113]. The uniaxial strain provided by (011) PZN-PT has been used to demonstrate electric-field-tuning of the ferromagnetic resonance (FMR) in magnetic FeGaB films. By adjusting the electric field strength the strength of the magnetoelastic anisotropy was tuned, which notably changed the measured FMR frequency due to the large magnetostriction of FeGaB [114–118]. The original FMR frequency is restored when the electric field is removed.

Tiercelin *et al* demonstrated a bistable magnetization state in zero applied electric field in an $TbCo_2$/FeCo substrate coupled to a piezoelectric (011) PZT stack [119]. By applying a constant external magnetic field perpendicular to a growth-induced uniaxial anisotropy axis, two stable magnetization states were

created 90° apart in the $TbCo_2$/FeCo stack. The strong fourfold magnetocrystalline anisotropy of epitaxial FeGa films has also been used to demonstrate non-volatile 90° magnetic switching in an applied electric field [120]. This resulted in a 90° switch of the magnetization state by applying either a positive or negative out-of-plane electric field pulse. Another mechanism that can provide deterministic electric-field-control of magnetic switching is exchange bias. Liu et al. have demonstrated that piezoelectric strain transfer from PZN-PT (011) substrates to FeMn/NiFe/FeGaB multilayers lead to near 180° rotation of the magnetization in an applied electric field [118]. Other proposals involve the use of bistable piezostrains of a partially poled (011) piezoelectric layer [121, 122]. Experimentally it has been shown that bistable in-plane piezostrains can be used for permanent magnetization switching in polycrystalline Ni films on (011) PMN-PT substrates [108]. Also, the hysteretic strain–voltage dependence of piezoelectric actuators has been used to demonstrate reversible electric field controlled switching of the remanent magnetization in polycrystalline Ni films [123].

Polarization reversal in a ferroelectric material is hysteretic. If the reversal process involves the nucleation and growth of ferroelastic domains, i.e. domains that are separated by non-180° domain walls, the lattice strain changes abruptly during ferroelectric switching. A hysteretic strain–voltage curve is obtained when the ferroelectric polarization rotates by less than 180°, which can be used to alter the magnetic properties of an adjacent magnetic film in a non-volatile manner. The maximum transferable strain from a ferroelectric substrate to a magnetic film depends on the ferroelectric material. As an example, $PbTiO_3$ and $BaTiO_3$ are both ferroelectric materials, but their tetragonal lattice elongations provide very different uniaxial strains of 6.4% and 1.1% respectively. Moreover, the strength of the magnetoelastic anisotropy induced by the ferroelectric substrate depends on the efficiency of strain transfer and the magnetoelastic properties of the magnetic film. Additionally, the symmetry of the induced magnetoelastic anisotropy depends on ferroelectric crystal structure, its orientation, and the direction of the polarization. Importantly, strain transfer from ferroelastic domains is laterally modulated. The induced magnetoelastic anisotropy in an adjacent magnetic film depends on the polarization direction in the underlying ferroelectric domain, which paves the way towards robust coupling between the orientation of local magnetoelastic anisotropy and the direction of ferroelectric polarization. The local characteristics of the strain transfer allows for the imprinting of ferroelectric domains into magnetic films and strong pinning of magnetic domain walls on top of ferroelectric domain

boundaries.

Structural phase transitions of $BaTiO_3$ substrates have been used to demonstrate strain coupling between a ferroelectric substrate and a magnetic film. The $BaTiO_3$ lattice undergoes changes from cubic to tetragonal at 393 K, tetragonal to orthogonal at 278 K and orthogonal to rhombohedral at 183 K [36]. These lattice transitions alter the strain state and thereby the magnetoelastic anisotropy of the magnetic film as indicated by abrupt jumps in magnetization. Macroscopic results have been obtained for $La_{1-x}Sr_xMnO_3$ [124, 125], Fe_3O_4 [126–128], Fe [129–134] and Sr_2CrReO_6 [135].

Electric-field-control of magnetism using $BaTiO_3$ substrates has been demonstrated in various magnetic films [129, 131, 133, 136, 137]. Eerenstein *et al* have demonstrated electric-field-control of magnetization in $La_{1-x}Sr_xMnO_3$ [125]. Applying an electric field in the different structural phases of $BaTiO_3$ resulted in abrupt changes to the magnetization as measured by VSM. Similar magnetic responses in an applied electric field have also been observed in Fe films [129, 134].

The macroscopic measurements discussed above do not provide information on the magnetic response on different ferroelectric domains. Due to the local strain transfer from ferroelastic domains, the change in magnetization varies from one domain to the other. Moreover, a variety of ferroelectric domain transformations can occur at the $BaTiO_3$ phase transitions, which complicates the interpretation of macroscopic data. The work presented in this thesis focuses on the imaging and measuring of ferroelectric–magnetic domain interactions using optical polarization microscopy. It is shown that these interactions result in domain pattern transfer from the ferroelectric substrates to the magnetic films. The magnetic domains are pinned on top of their ferroelectric counterparts, which enables electric-field-control of magnetic domain wall motion and local magnetization rotation in zero applied magnetic field.

5. Experimental Methods and Modeling

The ferroelectric substrate used throughout the study presented in this thesis is $BaTiO_3$, and the magnetic films grown on top are amorphous CoFeB, polycrystalline CoFe and epitaxial Fe. This chapter summarizes the growth methods and deposition conditions for each film material and sample characterization methods used.

5.1 Thin film growth

Three different strain-driven multiferroic heterostructure systems are investigated in this work, all of which utilize inverse magnetostriction. $BaTiO_3$ was chosen as the ferroelectric substrate material as it possesses a large c/a ratio of 1.1%. Ferromagnetic $Co_{60}Fe_{40}$ (CoFe), Fe and $Co_{40}Fe_{40}B_{20}$ (CoFeB) were selected as film materials: CoFe and CoFeB were chosen for their large magnetostrictions (λ_s) of 6.8×10^{-5} [138] and 3.5×10^{-5} [6] respectively to maximize the magnetoelastic anisotropy. Fe was selected because of its lattice-match with the $BaTiO_3$ substrate allowing for epitaxial growth of Fe on to $BaTiO_3$ substrates.

The CoFe films were grown onto 10 mm × 10 mm × 0.5 mm $BaTiO_3$ (001) substrates with $a_1 - a_2$ domain patterns at room temperature using electron beam evaporation (Section 5.1.1). These films had a polycrystalline texture, which reduces the magnetocrystalline anisotropy. Moreover, the composition of 60% Co and 40% Fe exhibits a low magnetocrystalline anisotropy [139]. Due to the minimal magnetocrystalline anisotropy the strain-induced magnetoelastic anisotropy fully dominates the magnetic properties of CoFe/$BaTiO_3$ (001)

To study the competition between magnetocrystalline and anisotropy in multiferroic heterostructures epitaxial, 10 nm and 20 nm thick Fe films were grown using molecular beam epitaxy (Section 5.1.2) onto 5 mm × 5 mm × 0.5 mm $BaTiO_3$ (001) substrates containing an $a - c$ domain structure. A requirement

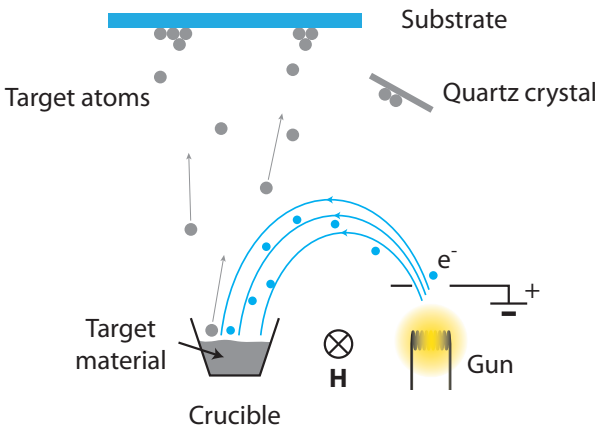

Figure 5.1. Electron beam evaporation utilizes a beam of electrons to heat a target material in a grounded crucible causing the material to sublime and condense on to a substrate placed opposite of the crucible.

for epitaxial film growth is a good lattice match between the substrate and film. Fe has a lattice parameter of 2.867 Å [6], which is a good match with $BaTiO_3$ if $Fe_{[110]} \parallel BTO_{[100]}$ ($a_{Fe\,[110]}$ = 4.059 Å c_{BTO}=4.035 Å a_{BTO}=3.991 Å). The Fe unit cell is compressed by 0.6% along the *c*–axis and 1.6% along the *a*–axis of the $BaTiO_3$ substrate.

CoFeB films were grown using magnetron sputtering (Section 5.1.3) onto 5 mm × 5 mm × 0.5 mm $BaTiO_3$ substrates with (011) oriented surfaces consisting of so-called *a*–*b* domains. The lateral uniaxial strains provided by the *a* and *b* domains are 1.1% and 0.55% respectively. The CoFeB film was grown as a wedge to study competition between magnetoelastic anisotropy and magnetostatic interactions between neighboring magnetic domains with increasing film thickness. The amorphous CoFeB films exhibit a negligible magnetocrystalline anisotropy.

5.1.1 Electron beam evaporation

Electron beam (e-beam) evaporation is a thin film deposition method conducted under vacuum conditions. A beam of electrons is created by thermionic emission from a W filament and directed towards a target material using a magnetic field. Figure 5.1 schematically illustrates a beam of electrons (e^-) from a W filament accelerated through a positively charged slit. The magnetic field, **H**, is perpendicular to the beam causing the electrons to adopt a trajectory towards the crucible. The electrons bombard the target material inside the crucible causing it to vaporize and condense onto the substrate placed opposite to the

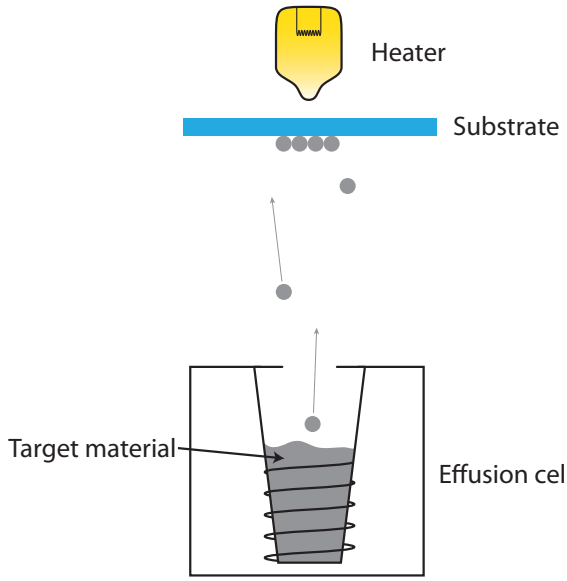

Figure 5.2. Schematic illustration of molecular beam epitaxy.

crucible. To prevent charging, the target and crucible both have to be conducting and grounded [140].

The deposition rate of electron beam evaporation is controlled by adjusting the current density of the electron beam. A quartz crystal microbalance is used to monitor the film thickness. A quartz crystal is oscillated at its resonance frequency, which depends on its surface properties. As the target material condenses onto the surface of the oscillating quartz crystal the resonance frequency changes, which is used to determine the thickness if the density and charge density of the film are known [141].

The samples prepared for this thesis by e-beam evaporation consisted of 15 – 20 nm CoFe films with a 3 nm Au capping layer to prevent oxidation. The films were grown at room temperature. The base pressure of the chamber before film deposition was $\sim 10^{-7}$ mbar and a liquid N_2 trap was used during outgassing of CoFe. A deposition rate of 0.1 – 0.2 nm/s was set before growth was initialized by opening a shutter plate above the crucible. The growth of smooth polycrystalline films was confirmed by x-ray diffraction and transmission electron microscopy.

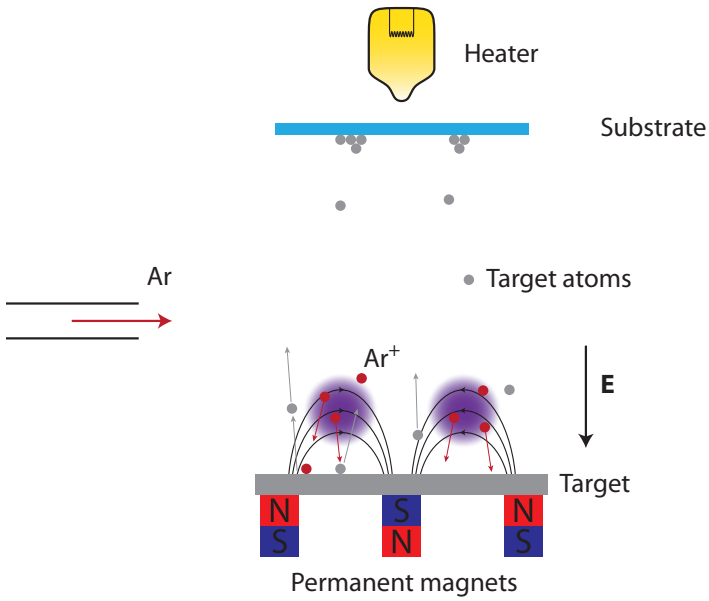

Figure 5.3. Schematic illustration of magnetron sputtering.

5.1.2 Molecular beam epitaxy

One popular method for producing crystalline films is molecular beam epitaxy (MBE). A crucible containing a target material is heated in an effusion cell, shown in Figure 5.2. The target material to sublimes, evaporating from the effusion cell and condensing onto the substrate surface and its surroundings [142–144].

MBE is conducted under high vacuum to prevent oxidation of the film material. The samples prepared by MBE consisted of 10 nm and 20 nm Fe films capped with 5 nm Au. The $BaTiO_3$ substrate was heated to 300 °C during growth to ensure epitaxy of the Fe film [145]. Transmission electron microscopy confirmed a $Fe_{[110]} \parallel BTO_{[100]}$ epitaxial relationship.

5.1.3 Magnetron sputtering

Magnetron sputtering uses a heavy-element plasma to bombard a target material, which vaporizes and condenses onto a diametrically located substrate, shown schematically in Figure 5.3. An inert process gas such as Ar continuously flows into the system, which is ionized by an electric field creating a plasma consisting of Ar^+-ions (indicated by red circles). The plasma is confined to a space above the target by magnetic fields generated by permanent magnets

underneath the target. If a ferromagnetic target is used the magnets in the gun have to be strong enough to overcome dipolar fields generated by the target. Applying a negative DC voltage on to the target material accelerates the Ar^+-ions towards the target (indicated by red arrows) causing target atoms (gray circles) to be knocked out. The vaporized target atoms form a plume, travelling through the atoms and ions in the chamber atmosphere performing a random-walk before condensing on to the substrate and chamber walls. Reactive gases such as O_2 can also be incorporated into the process gas to create oxides and other material mixtures [146–149].

A plasma can be maintained during sputtering at low pressures ($\sim 10^{-4}$ mbar) because the bombardment process continuously ionizes Ar atoms, which feed the plasma. To form the plasma a critical voltage, V_{crit}, is required to initiate the plasma formation process.

Two parameters control the rate of growth of the thin film; the process gas pressure and the voltage applied to the target. Using a higher process gas pressure increases the likelihood of ionization events which in turn decreases V_{crit}. However, an increase in pressure also decreases the mean free path of target atoms decreasing the growth rate. An increase in the voltage above V_{crit} increases growth rate as the Ar^+-ions gain more energy, which increases evaporation events on the target surface.

A mechanized shutter is used to control the exposure of the substrate to the vaporized target material. The shutter is closed during an initialization period where the production of the plasma is started and impurities on the target surface are evaporated. Once the initialization is complete the rate of evaporation is linear with time and therefore the film thickness is controlled by setting the total sputter time. The growth rate is calibrated by measuring the film thickness of a control sample using small-angle x-ray diffraction.

The CoFeB and Au targets used for sample preparation by magnetron sputtering were 2 inches in diameter with the target–substrate distance ~10 cm. The base pressure of the system before sputtering was $\sim 10^{-7}$ mbar. Ar was used as the process gas. An Ar flow of 30 sccm was used during deposition, which resulted in an Ar sputtering pressure of 6×10^{-3} mbar. The CoFeB film was grown as a wedge film from 0 nm to 110 nm thickness using a motorized shadow mask system, as schematically shown in Figure 5.4. During growth the mask was moved towards the direction indicated by the white arrow. This resulted in a linear increase of the CoFeB film thickness. The distance between the mask and substrate was ~3 mm. The power applied to the target was 50 W and 30 W, which resulted in growth rates of 0.16 nm/s and 0.2 nm/s for CoFeB

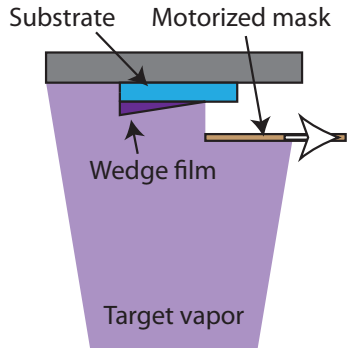

Figure 5.4. Schematic illustration of wedge film growth.

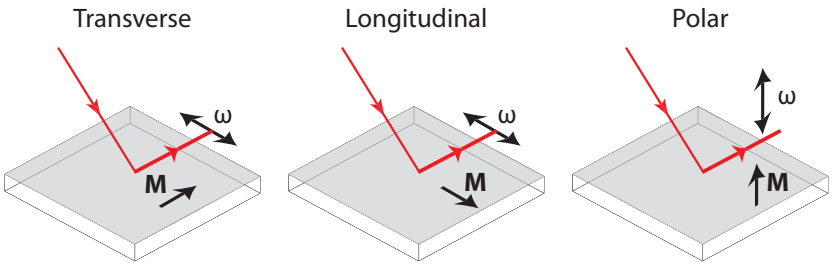

Figure 5.5. The three geometries of the magneto-optical Kerr effect; transverse, longitudinal and polar. Incident light is illustrated by the red line and **M** represents the direction of magnetization. The axis formed by the plane of incidence is indicated by ω.

and Au respectively. The $BaTiO_3$ substrate was heated above its Curie temperature to 200°C at 20°C/minute before film growth. The growth temperature was chosen to be below the crystallization temperature of CoFeB (≈350 °C [150]).

5.2 Magneto-optics

The magneto-optical Kerr effect (MOKE) is a phenomenon where reflected light interacts with a magnetic material, measured either as a change in optical polarization or light intensity. MOKE can also be used to image magnetic domains if used in conjunction with an optical microscope. A brief summary of MOKE and MOKE microscopy is presented here.

5.2.1 Magneto-optical Kerr effect

MOKE occurs in three geometrical configurations; transverse, longitudinal and polar, shown in Figure 5.5. When the magnetization is perpendicular to the direction of incident light propagation (i.e. perpendicular to the wave vector, **k**) the configuration is called transverse MOKE, which results in a small change in light intensity.

The polar and longitudinal MOKE configurations require a component of the magnetization to be oriented parallel to **k**. Here, the polarized light interacts with the spin-orbit interaction of electrons in magnetic materials. The samples in this thesis were characterized using the longitudinal MOKE configuration, where the magnetization lies in the plane of the sample. In the longitudinal MOKE configuration a non-zero angle of incidence is required for **k** to have a component in the plane of the sample [151, 152].

A polarizer–analyzer configuration is used to detect the rotation of optical polarization in the longitudinal configuration. In a polarizer–analyzer set-up the incident light is polarized using a polarizer. After reflection off the magnetic sample the light passes through a second polarizer, known as an analyzer, and its intensity is measured by a detector. If the polarizer and analyzer are at extinction (polarizing axes at 90° to one-another) and no optical polarization rotation is induced by the sample, an intensity minima will be measured. However, the interaction between the polarized light and the magnetic sample causes a rotation of the optical polarization resulting in a component of polarized light along the optical axis of the analyzer, which is detected as an increase in light intensity at the detector. The intensity change is proportional to the projection of the magnetization vector onto the axis formed by the plane of incidence, as indicated by ω in Figure 5.5.

5.2.2 Magneto-optical Kerr microscopy

A magneto-optical Kerr effect microscope is used to image magnetic domains (Zeiss Axio Imager.D2 polarization microscope modified by Evico for magneto-optical Kerr microscopy measurements). Figure 5.6 illustrates the configuration for longitudinal MOKE microscopy. White light passes through a slit forming a narrow beam of light, which is polarized and reflected off a beam splitter towards an objective lens. The slit is used to create a plane of incidence. The objective lens (either 20× or 100× magnification) focuses the light onto the sample surface where it is reflected back up through the beam splitter and analyzer to a CCD camera (Hamamatsu C4742-95), which detects local intensity changes. To

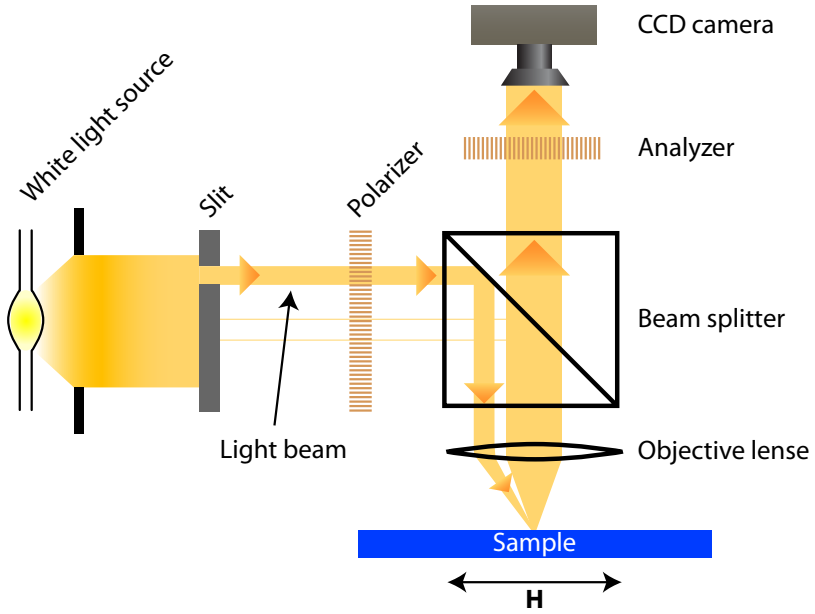

Figure 5.6. A schematic of a polarization microscope in MOKE configuration. **H** indicates the axis of the external magnetic field.

ensure that sufficient light arrives at the CCD camera, the analyzer is slightly rotated away from extinction.

A background imaging method is used to enhance contrast from magnetic domains. Here, a 5 Hz oscillating magnetic field is applied to the magnetic sample oscillating the magnetization from $-M_s$ to $+M_s$. A series of 16 images are captured and averaged whilst applying the oscillating magnetic field. The resulting averaged image is used as a background image. Subtraction of the background image from the live image removes static background information such as defects and ferroelectric domains. The resulting image contains only magnetic contrast.

Magnetic hysteresis curves constructed from MOKE images indicate the evolution of magnetic contrast during magnetization reversal. Local hysteresis curves are measured by pre-selecting an area in the microscope software, which measures an intensity change in the selected area only. The Faraday Effect causes the polarization of light to undergo a rotation when passing through a transparent material in a magnetic field parallel to the propagation direction. The rotation increases linearly with magnetic field strength and has to be taken into account when measuring a hysteresis curve with a MOKE microscope. In hysteresis measurements the Faraday Effect arises as a linear gradient once

the magnetic sample has reached M_s. The hysteresis curves presented in this thesis were obtained after subtraction of the Faraday Effect from the measurement data.

Ferroelectric domains can be imaged using an optical polarization microscope if the magnetic film on top of the $BaTiO_3$ substrate is semi-transparent for white light. Ferroelectric contrast originates from birefringence. Ferroelectric domains can be isolated from magnetic contrast by saturating the magnetic domains with an external magnetic field.

External magnetic fields are applied using an in-plane electromagnet. A shunt resistor is used to measure the electric current flowing through the electromagnetic, which is used to determine the magnetic field strength. The magnetic field generated by the electromagnet is calibrated using a Hall sensor.

5.2.3 Electric field and temperature measurements

Electric field experiments were performed on the $CoFe/BaTiO_3$ sample by applying an electric field perpendicular to the $BaTiO_3$ substrate whilst imaging ferroelectric and magnetic domains using the optical polarization microscope. An electric field sample holder was designed for use in the microscope (Figure 5.7). The sample was attached to a metal back plate using silver paste, which doubles as an electrode. The grounded metallic CoFe film on top of the substrate acts as the second electrode. A positive voltage was applied to the back plate. The voltage was ramped at 10 V/min to avoid substrate fracturing.

A continuous-flow liquid N_2 microscope cryostat (Janis ST-500) was used for temperature-control experiments (Figure 5.7). In this cryostat, thermal gel provides a good thermal contact between the sample and sample mount. The sample space is pumped down to 10^{-6} mbar during temperature-control experiments. A 50 Ω heater in conjunction with a LakeShore temperature controller is used to stabilize and control the sample temperature.

5.3 Magnetic modeling

A macrospin model and micromagnetic simulations were used to analyze domain pattern transfer and local magnetization reversal in multiferroic heterostructures. In the macrospin model the energy of two neighboring magnetic stripe domains are minimized in an iterative fashion. The orientation of the magnetoelastic anisotropy is orthogonal in neighboring domains and domain coupling is taken into account by magnetostatic and exchange energy terms.

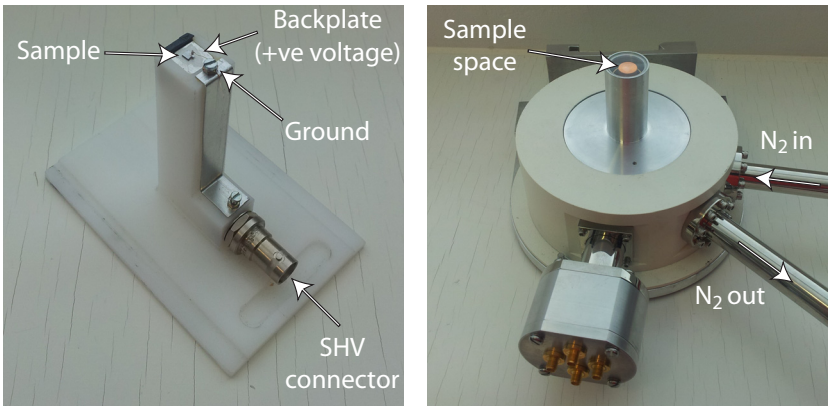

Figure 5.7. Optical polarization microscope sample holder used for electric-field experiments (left image) and microscope cryostat used for temperature control (right image).

For micromagnetic simulations the Object Oriented Micromagnetic Framework (OOMMF) software was used [153].

5.3.1 Macrospin model

A macrospin model was used to analyze the competition of magnetoelastic, shape, exchange and magnetostatic stray field energies in multiferroic heterostructures consisting of a $BaTiO_3$ substrate containing an a_1–a_2 ferroelectric domain pattern and a CoFe thin film. Strain transfer from the a_1 and a_2 domains in the $BaTiO_3$ substrate induce uniaxial magnetoelastic anisotropy in the CoFe film. The easy magnetoelastic anisotropy axes are orthogonal in neightboring domains, shown in Figure 5.8. Magnetization reversal in the uniaxial domains proceeds by coherent rotation and abrupt magnetization reversal. In the model the energies of two neighboring magnetic stripe domains are analyzed as a function of applied magnetic field. Besides the Zeeman energy the following anisotropy contributions are taken into account: Uniaxial magnetoelastic anistropy K_{me} due to interface strain coupling, uniaxial shape anisotropy K_{shape} due to the elongated shape of the stripe domains, exchange anisotropy K_{ex} and magnetostatic stray field anisotropy $\mu_0 H_{str} M_s$. The latter two anisotropies describe the ferromagnetic exchange and magnetostatic stray field coupling between domains. The total energies, E_1 and E_2 of the magnetic a_1 and a_2 domains, can be written as

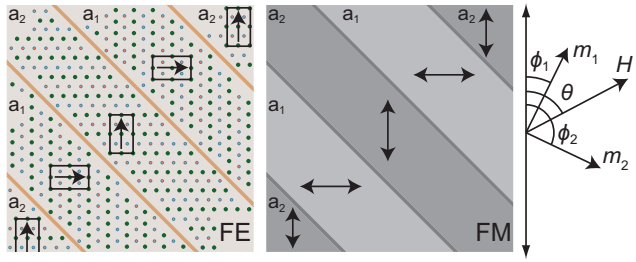

Figure 5.8. Top-view of ferroelectric $BaTiO_3$ domain structure (FE) and strain-induced magnetic domain pattern (FM). Arrows in FE indicate the direction of polarization and the double headed arrows in FM indicate the easy anisotropy axis. Angle definitions for the magnetization in a_1 and a_2 domains (ϕ_1 and ϕ_2) and the external magnetic field (θ) are given on the right.

$$\begin{aligned} E_1 = {} & K_{me}\cos^2\left(\phi_1\right) + K_{shape}\cos^2\left(\phi_1 - \frac{\pi}{4}\right) \\ & - K_{ex}\cos\left(\phi_1 - \phi_2\right) \\ & - \mu_0 H_{str} M \cos^2\left(\phi_2 - \frac{\pi}{4}\right)\cos\left(\phi_1 - \phi_2\right) \\ & - \mu_0 H_{ex} M \cos\left(\phi_1 - \theta\right), \end{aligned} \tag{5.1}$$

$$\begin{aligned} E_2 = {} & K_{me}\cos^2\left(\phi_2\right) + K_{shape}\cos^2\left(\phi_2 - \frac{\pi}{4}\right) \\ & - K_{ex}\cos\left(\phi_1 - \phi_2\right) \\ & - \mu_0 H_{str} M \cos^2\left(\phi_1 - \frac{\pi}{4}\right)\cos\left(\phi_1 - \phi_2\right) \\ & - \mu_0 H_{ex} M \cos\left(\phi_2 - \theta\right), \end{aligned} \tag{5.2}$$

where $\mu_0 H_{ex} M$ is the Zeeman energy. Energy minimizations of Equations 5.1 and 5.2 are performed by small iterations of the external magnetic field from $H_{ex} = H_{sat} \rightarrow -H_{sat}$. Polar plots of remanent magnetization as a function of the external magnetic field angle, θ, are constructed from the values of ϕ_1 and ϕ_2 at $H_{ex} = 0$.

The macrospin model reproduces the main magnetic features of the experimental samples when the widths of the stripe domains are larger than the width of the magnetic domain walls. Size-scaling effects that occur on very narrow ferroelectric stripe domains are not described by this model.

5.3.2 Micromagnetic simulations

Micromagnetic simulations are used to study magnetization reversal in multiferroic heterostructures and to analyze the intrinsic properties of pinned mag-

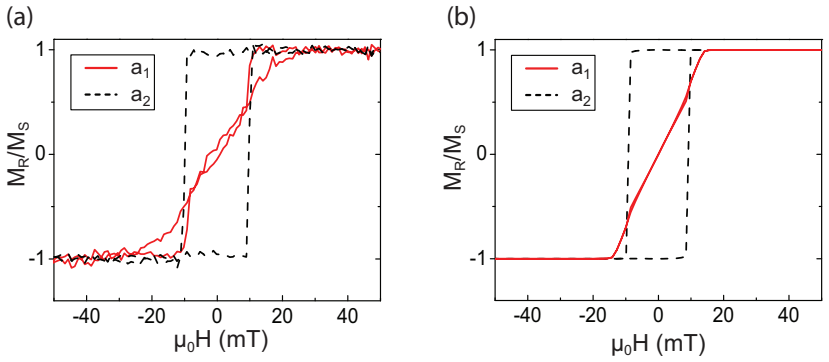

Figure 5.9. Measured (a) and simulated (b) magnetic hysteresis curves for the a_1 and a_2 domains of a CoFe film on top of $BaTiO_3$.

netic domain walls. The OOMMF software uses a 3-D mesh of finite-size elements to locate local minima in the energy landscape through direct minimization techniques during magnetization reversal in an external magnetic field. At every step of the external magnetic field OOMMF produces a matrix containing 3-D spin information of each individual element. The magnetization within the individual elements is assumed to be constant.

To simulate the experimental system made up of imprinted magnetic a_1–a_2 domains from a $BaTiO_3$ substrate, an alternating array consisting of 5 μm wide stripes with orthogonal uniaxial anisotropy axes was modeled. Periodic 2-D boundary conditions were used to minimize demagnetization fields at the edges of the simulated area [154]. For CoFe on $BaTiO_3$ the following input parameters were used: saturation magnetization $M_s = 1.7 \times 10^6$ A/m, exchange stiffness $K_{ex} = 2.1 \times 10^{-11}$ J/m and magnetoelastic anisotropy strength $K_{me} = 1.7 \times 10^4 J/m^3$. The value of K_{me} was determined from experiments on CoFe/$BaTiO_3$. A comparison of the measured and simulated hystresis curves for a CoFe film on $BaTiO_3$ is shown in Figure 5.9.

In the micromagnetic simulations it is assumed that the structure of the ferroelectric boundaries does not change during magnetization reversal in the magnetic film. The maximum strain that can be transferred from an isotropic CoFe film to a $BaTiO_3$ substrate via magnetostriction is given by $\varepsilon = 3/2\lambda_s(\cos^2\phi - 1/3)$ [6], where λ_s is the magnetostriction constant (6.8×10^{-5}) for $Co_{60}Fe_{40}$. Hence, the maximum strain for 90° magnetization rotation equals $3/2\lambda = 0.01\%$. Consequently, the strain that can be induced by CoFe is two orders of magnitude smaller than the lattice elongation of the $BaTiO_3$ substrate (1.1%). Therefore, magnetostriction does not provide sufficient elastic energy to significantly alter the ferroelectric domain walls of the $BaTiO_3$ substrate.

6. Results and Discussion

The first part of this Chapter discusses domain pattern transfer, magnetization reversal and magnetic domain wall pinning in various ferromagnetic-ferroelectric heterostructures. In the latter part of the Chapter electric field and temperature control of magnetic domain formation, local magnetization reversal and domain wall motion are presented.

6.1 Pattern transfer

In the tetragonal phase, $BaTiO_3$ exhibits a c/a ratio of 1.1%. In this phase the ferroelectric polarization is collinear with the elongated c-axis. Depending on the substrate orientation and polarization direction different ferroelastic patterns can be obtained. In the experiments we consider three different ferroelectric domain structures. These are a_1–a_2 and a–c domains (both in (001) oriented $BaTiO_3$, see Section 3.1.2) and a–b domains in (011) oriented $BaTiO_3$. The magnetic films prepared onto the $BaTiO_3$ substrates are $Co_{60}Fe_{40}$, $Co_{40}Fe_{40}B_{20}$ and Fe. A summary of pattern transfer results from Publications I, II, IV and V are presented in the following.

6.1.1 CoFe/$BaTiO_3$

The as-deposited state of magnetic CoFe films grown onto $BaTiO_3$ substrates containing a regular a_1–a_2 domain pattern are discussed in Publications I and II. Figure 6.1 (a) shows MOKE microscopy images of the ferroelectric domain pattern and the as-deposited magnetic domain pattern in zero applied magnetic field. The ferroelectric domain pattern is imprinted into the magnetic film via interface strain transfer: The lattice elongation of the ferroelectric a_1 and a_2 domains is partially transferred to the CoFe film, which induces local uniaxial magnetoelastic anisotropy axes via inverse magnetostriction. The positive magnetostriction of CoFe causes the easy anisotropy axes to align with the po-

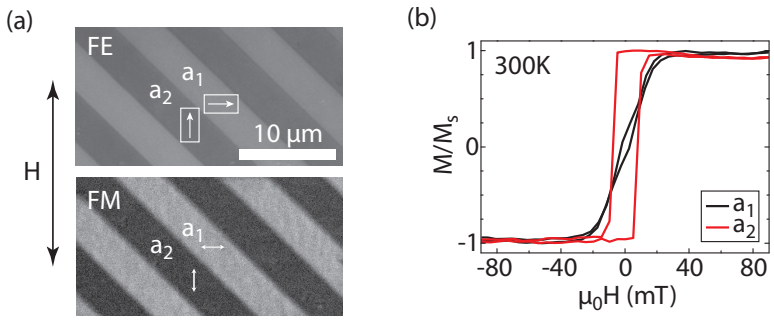

Figure 6.1. (a) MOKE microscopy images of ferroelectric (FE) and magnetic (FM) domains acquired at the same location of the CoFe/$BaTiO_3$ sample. Arrows in FE indicate the polarization direction and double headed arrows in FM indicate the anisotropy easy axis. (b) Local magnetic hysteresis curves measured along the axis indicated by H for a_1 and a_2 domains.

larization direction in the underlying ferroelectric domains.

Local MOKE microscopy hysteresis curves of the magnetic a_1 and a_2 domains, shown in Figure 6.1 (b), confirm the orthogonality of the easy anisotropy axes as verified by the easy- and hard-axis nature of the hysteresis curves. From the slope of the hard-axis hysteresis curve the magnetoelastic anisotropy is estimated as $K_{me} = 1.7 \times 10^4$ J/m^3. If we assume full strain transfer ($\varepsilon = -1.1\%$) and use $Y = 2.5 \times 10^{11}$J/m^3 [155] and $\lambda = 6.8 \times 10^{-5}$ [139] as the Young's modulus and magnetostriction of CoFe, Equation 2.7 gives $K_{me,max} = 2.8 \times 10^5$J/m^3. This suggests that less than 10% of the $BaTiO_3$ substrate lattice elongation is transferred during CoFe film growth. The low strain transfer efficiency is attributed to the polycrystalline nature of the films.

Figure 6.2 shows the angular dependence of the remanent magnetization, M_R/M_S, for a_1 and a_2 domains, attained from local MOKE microscopy hysteresis measurements. A maximum value for the remanent magnetization ($M_R/M_S \approx 1$) indicates the orientation of the magnetic easy axis of the a_1 and a_2 domains, reaffirming the orthogonality of the magnetic anisotropy axes of the two domains.

Anisotropy contributions

To analyze the different anisotropy contributions to the energy landscape of the a_1 and a_2 domains, the macrospin model is used to calculate polar plots of the remanent magnetization as a function of magnetic field direction (also discussed in Publication I). Figure 6.3 (a) shows the polar plot of the remanent magnetization of a_1 and a_2 domains when only uniaxial magnetoelastic anisotropy is taken into account. The polar plots of the individual stripe domains consist of two perfect circles. The easy axes are indicated by $M_R/M_S = 1$. Here,

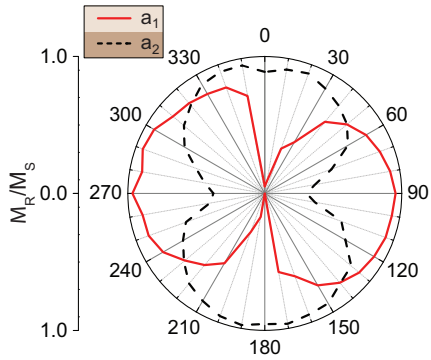

Figure 6.2. Polar plot of M_R/M_S as a function of θ ($\theta = 0$ lies along the H-axis indicated in Figure 6.1) for a_1 and a_2 domains in CoFe/$BaTiO_3$.

equal magnetoelastic anisotropy strength is assumed in both domains, which is only true if the domain widths are equal (a condition that is not fulfilled in the experimental samples).

Including magnetostatic shape anisotropy (shown in Figure 6.3 (b)) rotates the easy axes of the domains toward one-another in the direction of the elongated side of the stripe domains. Figure 6.3 (c) includes direct exchange coupling ($K_{shape}, H_{str} = 0$), both of which broaden the circles of the polar plot, and (d) includes magnetostatic stray field coupling ($K_{shape}, K_{ex} = 0$), which broadens and rotates the polar plots. Comparing the experimental results in Figure 6.2 to the macrospin model indicates that magnetoelastic anisotropy due to strain transfer is the dominant magnetic anisotropy contribution. However, some broadening and a small rotation of the experimental polar plots due to K_{ms}, K_{ex} and/or $\mu_0 H_{str} M_s$ can be observed.

Domain wall pinning

Images attained by MOKE microscopy in Figure 6.4 demonstrate magnetic domain wall pinning in the a_1–a_2 domain systems, where the magnetic domain walls are pinned onto the narrow ferroelectric domain boundaries of the $BaTiO_3$ substrate due to an abrupt 90° rotation of the magnetoelastic anisotropy axes (domain wall pinning is discussed in Publications III & IV). The pinning of the magnetic domain walls results in two main phenomena: (i) When the ferroelectric domain wall is moved by an electric field, the magnetic domain wall is dragged along. This effect enables direct electric field control of magnetic domain wall motion as demonstrated in Section 6.2. (ii) The magnetic domain walls do not move in an external magnetic field. As a result, the intrinsic properties of pinned domain walls (spin-rotation, chirality, width) can be tuned by an external magnetic field. The application of a magnetic field perpendicular

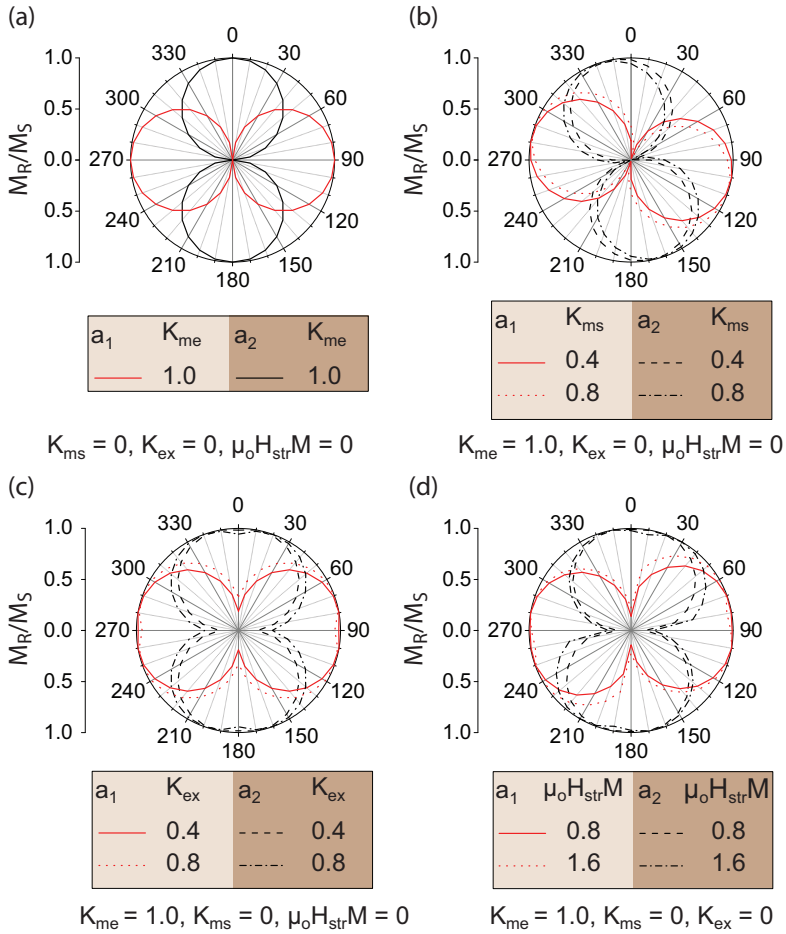

Figure 6.3. Simulated polar plots of M_R/M_S as a function of θ for a_1 and a_2 domains using Equations 5.1 and 5.2. The contribution of (a) K_{me}, (b) K_{me} and K_{ms}, (c) K_{me} and K_{ex} and (d) K_{me} and $\mu_0 H_{str} M_s$ are compared.

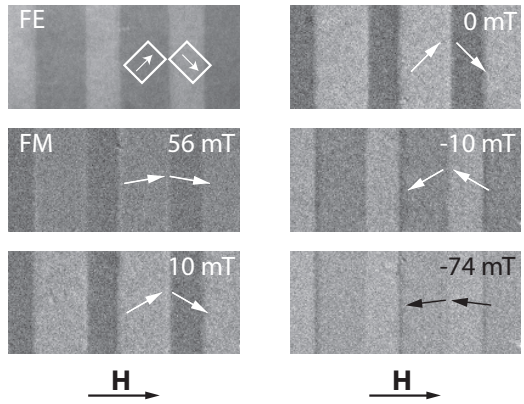

Figure 6.4. Ferroelectric (FE) domain image and magnetic (FM) domain images as a function of magnetic field strength for CoFe/$BaTiO_3$. The magnetic domain walls do not move due to strong pinning on to the ferroelectric domain boundaries.

to the domain walls results in the formation of narrow uncharged walls, while broad charged domain walls form when a field is applied parallel to the walls. Figure 6.5 shows the remanent magnetic spin structure after applying magnetic fields in these two field directions. The width of the domain wall is about an order magnitude larger for the charged domain walls due to an additional magnetostatic contribution to the domain wall energy (shown in Figure 6.5 (c)). Besides the width, the spin rotation in domain walls can also be tuned by variation of the magnetic field strength (shown in Figure 6.5 (d)).

6.1.2 Fe/$BaTiO_3$

The competition between magnetocrystalline and magnetoelastic anisotropies with laterally modulating symmetry is studied in epitaxial Fe films grown onto $BaTiO_3$ substrates containing *a*–*c* domains, schematically illustrated in Figure 6.6 (a). Transmission electron microscopy measurements confirm growth of epitaxial Fe films on top of $BaTiO_3$ with $Fe_{[110]} \parallel BTO_{[100]}$ [Publication IV]. Through strain transfer at the substrate–film interface the crystalline Fe film is laterally compressed by the ferroelectric domains. The ferroelectric *a*–domains compress the Fe lattice by 1.6% and 0.6% in the $[\bar{1}10]_{Fe}$ and $[110]_{Fe}$ directions respectively, creating a local uniaxial magnetoelastic easy axis parallel to the domain wall. The ferroelectric *c*–domains compress the Fe lattice biaxially along $[110]_{Fe}$ and $[\bar{1}10]_{Fe}$ by 1.6%. The 1.6% compression is not sufficient to overcome the magnetocrystalline anisotropy of Fe (see Section 2.3.1). Hence, the magnetization easy axes in the *c*–domains lie along $\langle 100 \rangle_{Fe}$ which are fa-

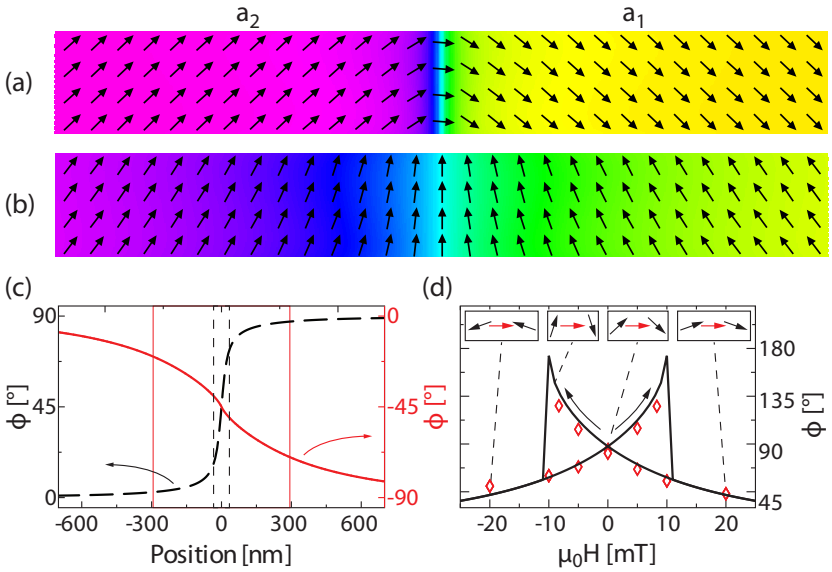

Figure 6.5. Micromagnetic simulations of (a) uncharged and (b) charged domain walls. (c) By measuring the spin rotation across the two types of domain walls at zero applied magnetic field the widths of domain walls can be determined. The uncharged wall (black dashed line) is about one order of magnitude narrower than the charged domain wall (red line). The domain wall width is determined using Equation 2.16. (d) Spin rotation within the domain walls as a function of magnetic field strength. The black line indicates the spin rotation, which is determined from micromagnetic simulations and the red dots represent experimental data.

vored by the magnetocrystalline anisotropy of Fe.

The angular dependence of the magnetic switching field of both *a*– and *c*–domains are shown in Figure 6.6 (c). It is apparent that the switching events in both domains occur simultaneously indicating coupling between neighboring domains. For example, a small abrupt magnetization switch is observed in the *a*–domain when measuring a hysteresis curve along its hard anisotropy axis, although purely coherent rotation is expected to contribute to the magnetization reversal at this field angle. The abrupt switch in the *a*–domain coincides with a switch of the magnetization in the *c*–domain. This suggests that inter-domain coupling via magnetostatic stray fields and exchange interactions trigger abrupt magnetization rotation in the *a*–domain when the *c*–domain switches.

Similarly, hysteresis curve measurements along the easy anisotropy axis of the *a*–domain demonstrates simultaneous switching of both domains. Here, the increase of the switching field suggests that the *a*–domain delays magnetic switching in the *c*–domain to minimize exchange energy. Furthermore, magnetization reversal along the easy anisotropy axis of the *c*–domain shows two simultaneous magnetization switching events in both domains. Around this field angle both domains contribute to the magnetization switching events; a first switch occurs simultaneously at a lower magnetic field strength, which is caused by the *c*–domains. A second magnetization switch occurs at a higher field strength, which is induced by the *a*–domains. For more information see Publication V.

6.1.3 CoFeB/$BaTiO_3$

A wedge film of magnetic $Co_{40}Fe_{40}B_{20}$ (0 nm – 110 nm thick) was grown onto a $BaTiO_3$ (110) substrate with *a*–*b* stripe domains to study the thickness dependence of ferroelectric-ferromagnetic domain pattern transfer in a strain mediated multiferroic heterostructure. The film was grown at 200°C, i.e. in the paraelectric cubic phase of $BaTiO_3$. At room temperature the uniaxial lattice strain provided by the *a*– and *b*–domains amounts 1.1% and 0.55% respectively.

The ferroelectric stripe domain pattern and magnetic domain structure at zero applied magnetic field are shown in Figure 6.7. The domain images demonstrate that the ferroelectric domain pattern is fully transferred to the CoFeB wedge in the entire film thickness range. Experimentally extracted polar plots of the remanent magnetization as a function of magnetic field angle show a rotation of the magnetic easy axes towards each other with increasing film thickness. The rotation of the easy axis is summarized in Figure 6.8 (a). Fur-

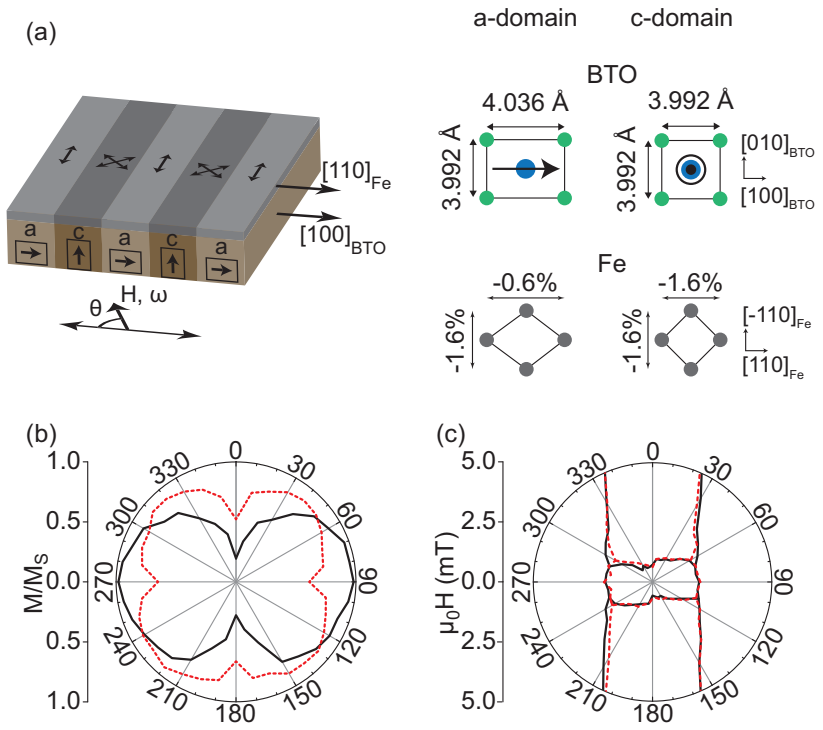

Figure 6.6. (a) Schematic of the Fe/$BaTiO_3$ system with angle definitions. Arrows indicate the direction of polarization in the $BaTiO_3$ substrate and double headed arrows indicate easy anisotropy axes in Fe. The $BaTiO_3$ and Fe lattices are shown on the right. The relative compression of the Fe lattice with respect to the bulk structure on the *a*– and *c*–domains of the $BaTiO_3$ substrate is indicated. (b) Remanent magnetization and (c) switching fields as a function of magnetic field angle (θ) for magnetic *a*– and *c*–domains.

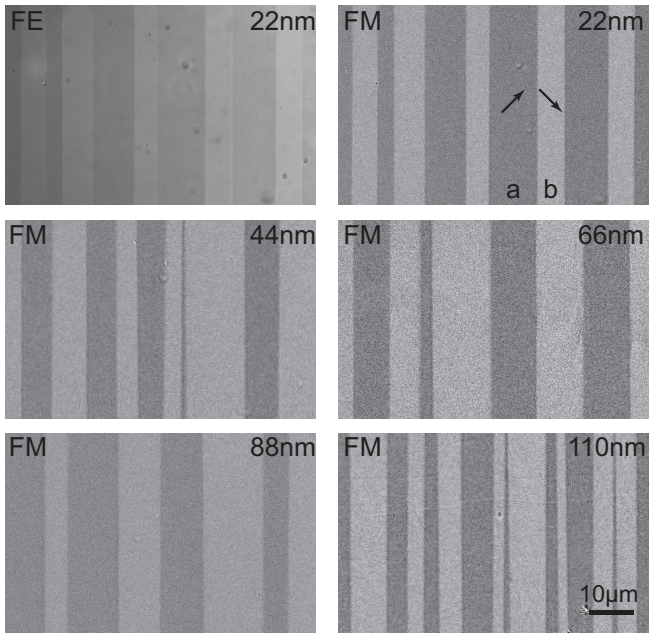

Figure 6.7. MOKE microscopy images of the ferroelectric domain pattern (FE) in the $BaTiO_3$ substrate and the imprinted domain structure of the CoFeB wedge (FM) for different film thickness in zero applied magnetic field. The arrows indicate the direction of magnetization in the a– and b–domains.

thermore, the uniaxial anisotropy strengths of the magnetic a– and b–domains are determined from hard-axis hysteresis measurements. The uniaxial anisotropy remains large up to 110 nm thick films (Figure 6.8 (b)). In fact, the uniaxial anisotropy constant increases with film thickness, which can be attributed to an increase in the magnetoelastic coupling coefficient, B, where $K_{me} \propto B(t)\varepsilon$ [22, 156, 157].

Using the macrospin model introduced in Section 5.3.1, rotation of the magnetic easy axes can be modeled assuming a linear increase of magnetostatic stray field interactions between a– and b–domains with increasing film thickness (solid lines in Figure 6.8 (a)). The following experimentally determined anisotropy values were used as input parameters: $K_u^a = 2.6 \times 10^3 + 0.7 \times 10^{10} \times t$ J/m^3 and $K_u^b = 1.3 \times 10^3 + 2 \times 10^{10} \times t$ J/m^3, leaving the magnetostatic energy as the only fitting parameter. Good agreement between the experimental data and model calculations is obtained for $H_{str} = 2.5 \times 10^{10} \times t$ A/m (solid lines in Fig 6.8 (a)), illustrating that magnetostatic stray field interactions between domains induce the rotation of the anisotropy axes with increasing film thickness. Extrapolation of the data suggests that magnetostatic stray field coupling will lead to a breakdown of the imprinted domain pattern for large magnetic film thicknesses ($t > 110$nm).

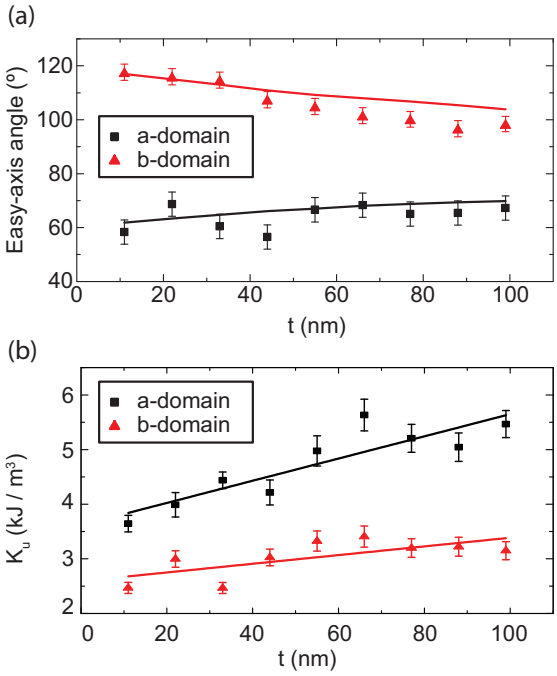

Figure 6.8. (a) Angle of the easy magnetization axis and (b) uniaxial magnetic anisotropy as a function of CoFeB film thickness. Solid lines in (a) are fits using the macrospin model (Equations 5.1 & 5.2). In this model, a linear increase of the magnetostatic stray field anisotropy with film thickness is assumed. The experimentally determined values for K_u are used.

6.2 Electric field control of magnetization and magnetic domain wall motion

The CoFe/$BaTiO_3$ samples discussed in Section 6.1.1 were the subject of a study on electric field manipulation of magnetic anisotropy experiments [Publication I, II, III]. First, a 10 kV/cm electric field was applied out-of-plane creating a single c–domain in the $BaTiO_3$ substrate. Reverting back to electric remanence causes a–domains to nucleate in the $BaTiO_3$ substrate creating an alternating a_1–c domain structure. Figure 6.9 shows the evolution of ferroelectric and magnetic domains from (a) the as-deposited a_1–a_2 domain state to (b) the a_1–c domain state after the application of an electric field. The ferroelectric domains widen and the domain boundaries rotate by 45° during the a_1–a_2 → a_1–c transition. The magnetic domain structure on top of the ferroelectric a_1–c pattern (shown in Figure 6.9 (b) FM) is a superposition of the as-deposited magnetic a_1–a_2 domain state and the electric-field-induced a_1–c domain structure. The as-deposited stripe domain pattern is retained on the ferroelectric c–domain creating two new magnetic domains labeled $a_{1,c}$ and $a_{2,c}$. Remnants of the as-deposited a_1–a_2 pattern are also visible on the ferroelectric a_1–domain in Figure 6.9 (b) FM, labeled $a_{1,a}$ and $a_{2,a}$. However, on the electric-field-induced a_1–domain, the contrast between the magnetic $a_{1,a}$ and $a_{2,a}$ is greatly reduced in zero applied magnetic field. Polar plots of the remanent magnetization for the $a_{1,c}$, $a_{2,c}$, $a_{1,a}$ and $a_{2,a}$ magnetic domains are shown in Figure 6.9 (c). The magnetic $a_{1,c}$ and $a_{2,c}$ domains retain their orthogonal magnetic easy axes. The magnetic $a_{1,a}$ and $a_{2,a}$ domains now exhibit collinear magnetic easy axes. To understand the underlying mechanisms behind electric field induced manipulation of local magnetic anisotropies, a more detailed analysis is given below.

Figure 6.10 summarizes the magnetic properties of the as-deposited (a_1 and a_2) and electric-field-induced ($a_{1,c}$, $a_{2,c}$, $a_{1,a}$ and $a_{2,a}$) magnetic domains. Hard axis hysteresis curves for the magnetic $a_{1,c}$ and $a_{2,c}$ domains indicate an increase of the uniaxial anisotropy strength from the as-deposited state (1.7×10^4 J/m^3) to the electric-field-induced state (1.3×10^5 J/m^3) which clearly indicates a high strain transfer efficiency during ferroelectric polarization reversal. Furthermore, the anisotropy axes of the magnetic stripe domains rotate by 90° in the electric-field-induced state.

The improved strain transfer efficiency in the electric-field-induced state is explained by film clamping. In the as-deposited state, strain transfer from the substrate to the magnetic film is weak due to strain relaxation (<10% during CoFe deposition). Once the film is deposited it is clamped to the substrate

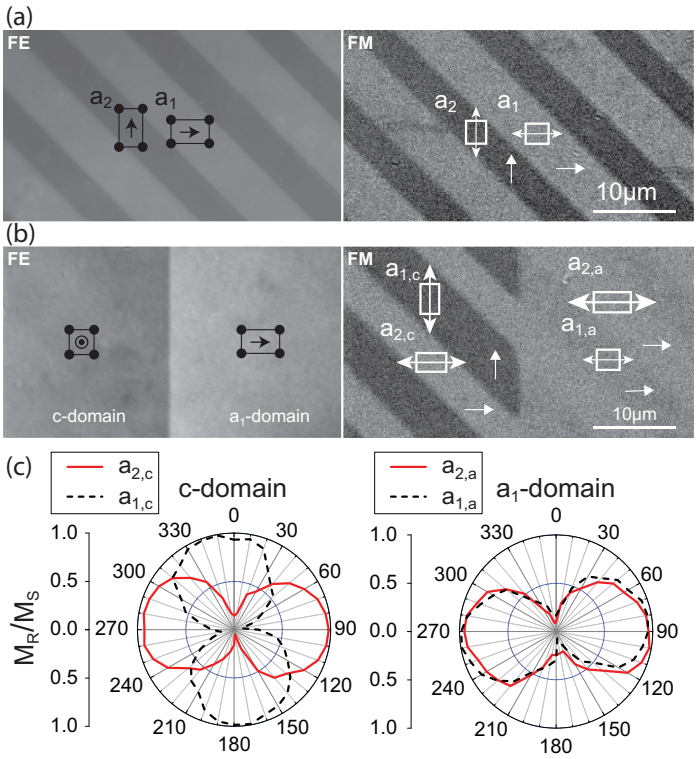

Figure 6.9. (a) The as-deposited domain state and (b) the *a*–*c* domain state after poling a $CoFe/BaTiO_3$ structure with an out-of-plane electric field. The images show the ferroelectric (FE) and magnetic (FM) domains in their remanent states. (c) Polar plots of the normalized remanent magnetization of the $a_{1,c}$, $a_{2,c}$, $a_{1,a}$ and $a_{2,a}$ domains measured on top of the ferroelectric *a* and *c* domains.

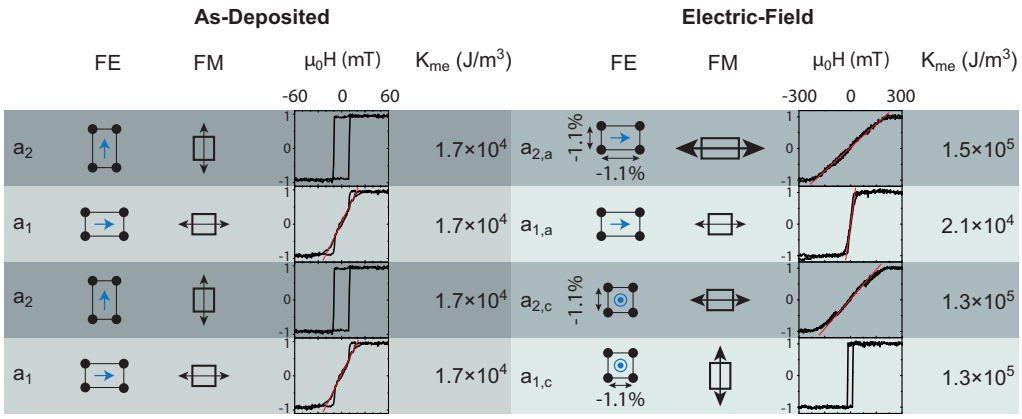

Figure 6.10. Magnetoelastic anisotropy strengths summarized for the as-deposited state a_1 and a_2 domains and electric-field-induced $a_{1,a}$, $a_{2,a}$, $a_{1,c}$ and $a_{2,c}$ magnetic domains.

leading to improved strain transfer efficiency. Therefore, electric-field-induced changes to the ferroelectric domain pattern lead to larger magnetoelastic anisotropies in the CoFe film.

On the electric-field-induced c–domain, the CoFe film is compressed locally with greater efficiency along the axis it gained a small tensile strain during deposition. The small as-deposited tensile strain ($\sim +0.1\%$) is therefore replaced by a large compressive strain (-1.1%), which results in the rotation the magnetoelastic anisotropy axes and a significant increase of the anisotropy strength. As the magnetization of both a_1 and a_2 domains rotate by 90°, the original magnetic stripe pattern is preserved on top of the ferroelectric c–domains.

Local magnetic measurements on the magnetic $a_{1,a}$ and $a_{2,a}$ domains indicate differing magnetoelastic anisotropy strengths. The $BaTiO_3$ lattice structure under the $a_{1,a}$ domain does not change during the application of an electric field. This is reflected by a small magnetoelastic anisotropy strength (2.1×10^4 J/m^3). However, under the magnetic $a_{2,a}$ domains, the ferroelectric a_2 domains are replaced by a_1 domains through a 90° polarization rotation in the substrate plane. This results in a -1.1% lattice compression and a $+1.1\%$ lattice elongation in two orthogonal directions, which causes the magnetoelastic anisotropy axis and the magnetization to rotate by 90°. In addition, the strength of the anisotropy increases significantly (1.5×10^5 J/m^3) due to efficient strain transfer in the electric field experiment.

Electric-field-induced magnetic domain wall motion is demonstrated in Figure 6.11. At 0 V the $BaTiO_3$ substrate contains an a_1–c domain pattern. The application of an electric field increases the c–domains at the expense of a_1–

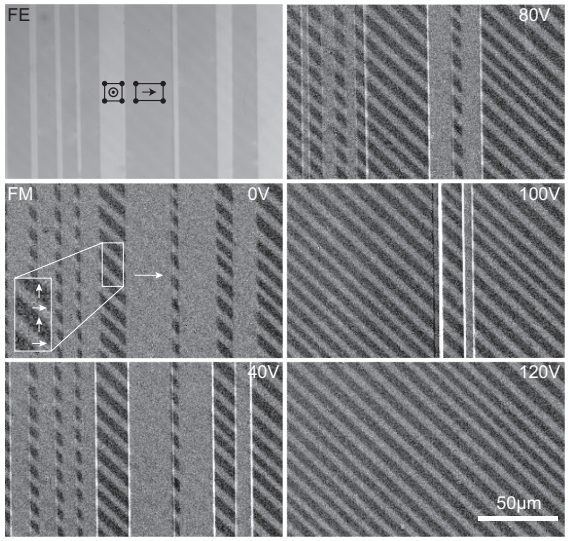

Figure 6.11. Magnetic domain wall motion induced by an electric field. Ferroelectric (FE) and magnetic (FM) domain states at 0V – 120V indicate the writing of magnetic stripe patterns by lateral magnetic domain wall motion. All images are acquired with $H_{ex} = 0$.

domains by lateral ferroelectric domain wall motion. The magnetic domain walls, which are pinned onto the ferroelectric domain boundaries by abrupt changes in the magnetoelastic anisotropy, are dragged along. Furthermore, the magnetic $a_{1,c}$ and $a_{2,c}$ stripe domains are rewritten because the motion of the ferroelectric boundary changes the local magnetic anisotropy of the CoFe film. This is a reversible process, whereby the magnetic $a_{1,c}$ and $a_{2,c}$ domain pattern is erased by the formation of ferroelectric a–domains once the electric field is removed. The data in Figure 6.11 demonstrates for the first time that magnetic domain wall motion can be fully controlled by an electric field without the need for an external magnetic field. Traditionally, magnetization rotation and magnetic domain wall motion are induced by an external magnetic field or an electric current through a magnetic nanowire. The ability to erase and rewrite domain patterns and to move magnetic domain walls by purely electrical means opens up routes towards electrically controllable low power magnetic devices.

6.3 Temperature control of magnetic anisotropy

Structural phase changes in $BaTiO_3$ can also be used to locally strain a magnetic film (as described in Section 6.1.1). Temperature induced magnetic domain control is demonstrated in samples consisting of CoFe films grown onto

$BaTiO_3$ substrates [Publication VI].

In the experiments, the magnetic domains are imaged using MOKE microscopy while temperature cycling the $BaTiO_3$ substrate through its rhombohedral (R), orthorhombic (O), tetragonal (T) and cubic (C) phases. Figure 6.12 shows the magnetic domain structure in zero applied magnetic field and hysteresis curves before and after the temperature induced structural phase transitions. To begin, the CoFe/$BaTiO_3$ sample with an a_1–a_2 domain pattern was cooled from room temperature through the T → O phase transition. Magnetic contrast images in Figure 6.12 show that the contrast in the magnetic domains is reversed indicating a 90° rotation of the magnetization direction during cooling ($300K \rightarrow 270K$). Figure 3.2 shows that cooling $BaTiO_3$ from room temperature to the orhtorhombic phase compresses the CoFe lattice along the *c*–axis. The direction of lattice compression is parallel to the small tensile strain that was obtained during CoFe film growth on tetragonal $BaTiO_3$. Furthermore, the CoFe film is slightly elongated along the *b*–axis. Due to film clamping, strain transfer during cooling is about one order of magnitude more efficient than during growth. Hence, the strain in the magnetic domains evolves from a weak tensile strain to a strong compressive strain, which causes the magnetoelastic anisotropy axes to rotate by 90°. Additionally to a rotation of the anisotropy axes, the saturation field of the hard axis hysteresis curve increases from 20 mT in the tetragonal phase to 170 mT in the orthorhombic phase, increasing the uniaxial anisotropy strength from 1.7×10^4 J/m^3 to 1.4×10^5 J/m^3, reaffirming the increase in strain transfer efficiency.

Cooling the sample through the O → R phase transition does not change the magnetic contrast of the domain pattern (Figure 6.12 250K → 170K). As a result of this phase transition the rhombohedral phase locally compresses the CoFe film along the *c*–axis, whilst decreasing the local tensile strain along the *b*–axis. Hence, only a small increase in magnetic anisotropy strength is observed (saturation field 170mT → 200mT).

Upon heating the sample from the tetragonal phase to the cubic phase of the $BaTiO_3$ substrate, the magnetic contrast is again reversed (Figure 6.12, 300 K → 420 K). Similarly to the T → O phase transition, the $BaTiO_3$ lattice compresses the CoFe film locally along the *c*–axis in the cubic phase. Futhermore, the cubic phase of $BaTiO_3$ induces a tensile strain along the *b*–axis in the CoFe film. Due to film clamping this results in a 90° rotation of the magnetic anisotropy axes. Unlike the abrupt T → O and O → R phase transitions, the $T \rightarrow C$ transition is gradual taking place over a temperature range of 320 K to 420 K. From 360 K to 390 K the growth-induced uniaxial tensile strain in the CoFe

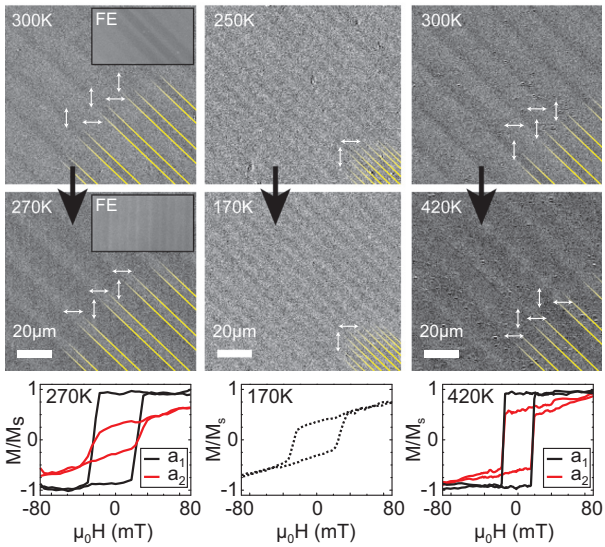

Figure 6.12. Images of CoFe domain structure at remanent magnetization before and after the phase changes of the $BaTiO_3$ substrate. During the 300 K → 270 K (T → O) and 300 K → 420 K (O → C) phase transitions, the magnetic contrast is reversed in the domains indicating 90° magnetization rotation at 300 K and 270 K (ferroelectric domain patterns are shown in the insets). Hysteresis curves measured on the magnetic a_1 and a_2 domains at 270 K (O) and 420 K (T) and a global hysteresis curve measured at 170 K (R) are also shown.

film is overcome by temperature induced compressive strain. After rotation of the uniaxial anisotropy axes, the strength of the anisotropy increases with temperature.

Ferroelectric domain changes in the tetragonal phase can be induced by repeated temperature cycling through T → O → T. Images in Figure 6.13 show the ferroelectric and magnetic domain patterns in the tetragonal phase at the same sample location (a) before and (b) after one and (c) two temperature cycles. The magnetic domain structure is shown at $H_{ex} = 0\,mT$ and $\pm 30\,mT$. In the as-deposited state, a one-to-one correlation between the ferroelectric and magnetic domains is observed. Here, both the a_1 and a_2 magnetic domains are fully saturated by $H_{ex} = 30\,mT$. After one temperature cycle (T → O → T) a ferroelectric a_2 domain is replaced by an a_1 domain, indicated by (1). Magnetically the area at (1) exhibits easy axis behavior in the as-deposited state. However, after the local ferroelectric $a_2 \rightarrow a_1$ domain change the magnetization exhibits hard axis behavior, which indicates a 90° rotation of the magnetoelastic anisotropy axis. Furthermore, the magnetization at location (1) no longer saturates at ±30 mT, indicating an increase of the magnetoelastic anisotropy strength. After a second temperature cycle two more $a_2 \rightarrow a_1$ domain changes

occur (indicated by (2)). Again, rotations of the magnetoelastic anisotropy axes are observed at these locations along with an increase in magnetoelastic anisotropy strength. The saturation fields for the new stripe domains is 600 mT, which gives $K_{me} = 5.1 \times 10^5\, J/m^3$, a value that is almost $2K_{me,max}$ (see Section 6.1.1). This is expected for full strain transfer as the CoFe film is compressed by -1.1% and elongated by +1.1% in two orthogonal directions. Finally, an a_2 domain grew in size leading to a rotation of the magnetoelastic anisotropy axis from hard axis to easy axis at (3). Again, a 90° rotation of magnetoelastic anisotropy axis is observed with rotation of the underlying ferroelectric polarization.

The underlying mechanism for the rotation and strengthening of the uniaxial anisotropy axis has been discussed in detail in Section 6.2. During deposition, strain transfer from the $BaTiO_3$ substrate to the CoFe film is weak. If a ferroelectric domain change ($a_1 \rightarrow a_2$ or $a_2 \rightarrow a_1$) is induced after deposition, much larger strains are transferred to the magnetic film. The ferroelectric domain change induces a -1.1% compression and a 1.1% elongation in two orthogonal directions. This results in a 90° rotation of the magnetoelastic anisotropy axes and an increase of the magnetoelastic anisotropy strength.

Although local changes to the ferroelectric domain pattern result in changes of the magnetoelastic anisotropy strength, the magnetic domain pattern at zero applied magnetic field always matches the underlying ferroelectric domains (if the ferroelectric polarization is in-plane). This provides a direct link between the direction of the polarization and magnetoelastic anisotropy, which can be utilized in future electric field controlled magnetic structures.

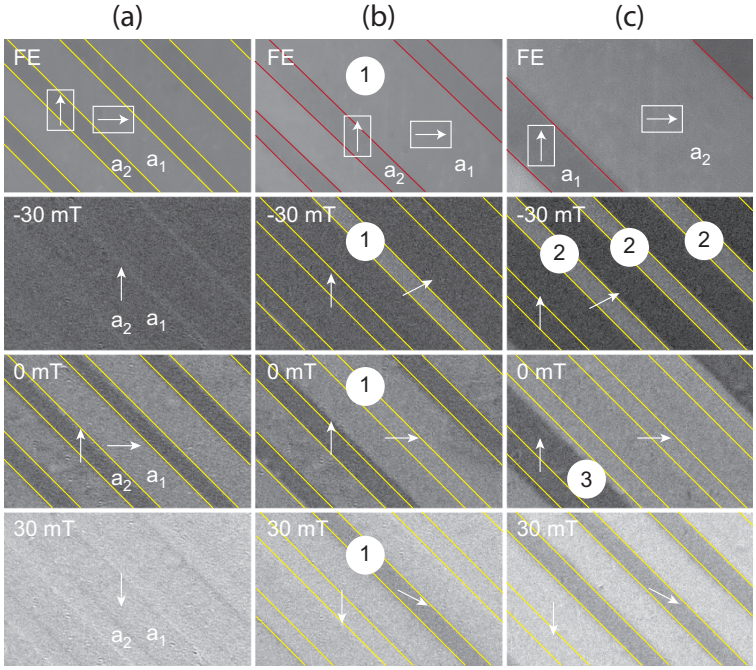

Figure 6.13. Polarization microscopy images of the FE and ferromagnetic domain structure at 300 K (tetragonal $BaTiO_3$). The images represent (a) the as-deposited state, (b) after one temperature cycle to orthorhombic $BaTiO_3$, and (c) after a second temperature cycle. The yellow lines in the images indicate the domain pattern of the $BaTiO_3$ substrate after CoFe film growth. The red lines in (b) and (c) illustrate the modified $BaTiO_3$ domain structure after temperature cycling. The arrows indicate the polarization direction in the $BaTiO_3$ substrate and the direction of magnetization in the CoFe film. The numbers label the areas in which the in-plane polarization of the $BaTiO_3$ substrate rotates by 90°.

7. Conclusions

Ferroelectric-ferromagnetic domain coupling in multiferroic heterostructures has been studied using optical polarization microscopy techniques. The results presented in this thesis demonstrate three major developments in the control of magnetic domains in strain-mediated multiferroic heterostructures: Firstly, it was shown that non-180° ferroelectric domain patterns in $BaTiO_3$ substrates are fully transferable to several different types of magnetic films through interfacial strain transfer and inverse magnetostiction. Secondly, electrical control of magnetization rotation and magnetic domain wall motion were achieved due to strong coupling between the magnetic and ferroelectric domains. Finally, during temperature-induced structural phase transitions in the $BaTiO_3$ substrate the magnetization of the magnetic film closely follows the in-plane rotation of the ferroelectric polarization.

Ferroelectric pattern transfer was demonstrated in multiferroic heterostructures using three different magnetic films: Magnetic polycrystalline CoFe, epitaxial Fe and amorphous CoFeB films all exhibited domain imprinting from ferroelectric $BaTiO_3$ substrates. Strain transfer from the regular, non-180° ferroelectric domain structures creates a well-defined magnetic domain pattern in the magnetic films. Abrupt in-plane rotations of the magnetoelastic anisotropy axes at ferroelectric domain boundaries forms pinning sites for the magnetic domain walls, immobilizing them during magnetization reversal. This well-defined, controllable magnetic domain structure provides the ability to tune magnetic domain properties, such as spin rotation and domain wall width, using an external magnetic field. Such magnetic domain patterns can be used as a basis to study a variety of different magnetic phenomenon including magnetic domain wall resistance and magnon propagation through magnetic domain walls.

Strong coupling of the magnetic domains to their ferroelectric counterparts was used to demonstrate electrical control of magnetization in $CoFe/BaTiO_3$.

The motion of ferroelectric domain boundaries in an applied electric field caused the pinned magnetic domain walls to be dragged along resulting in electric-field-induced propagation of magnetic domain walls. For the first time, electric field controlled magnetic domain wall motion and local magnetization rotations have been demonstrated, providing a platform to study domain coupling and magnetic domain wall motion in more intricate multiferroic heterostructures.

Understanding the microscopic phenomenon in multiferroic heterostructures can pave the way towards low energy magnetic actuators and spintronic devices. The in-depth analysis of magnetization reversal processes – including domain coupling and the effects of inter-domain interactions – and electric-field-induced magnetic domain wall motion have provided new insights into the physics of electric field controlled magnetism. This provides a foundation for studies on electric field control of local magnetization in multiferroics consisting purely of thin film structures, miniaturized multiferroic systems and electric field control of domain wall logic devices.

Bibliography

[1] N. A. SPALDIN and M. FIEBIG, *Science* **309**, 391 (2005).

[2] J. STÖHR and H. C. SIEGMANN, *Magnetism: From Fundamentals to Nanoscale Dynamics*, Springer, 2006.

[3] S. BLUNDELL, *Magnetism in Condensed Matter*, Oxford University Press, 2010.

[4] C. L. DENNIS, R. P. BORGES, L. D. BUDA, U. EBELS, J. F. GREGG, M. HEHN, E. JOUGUELET, K. OUNADJELA, I. PETEJ, I. L. PREJBEANU, and M. J. THORNTON, *Journal of Physics: Condensed Matter* **14**, R1175 (2002).

[5] C. A. F. VAZ, J. A. C. BLAND, and G. LAUHOFF, *Reports on Progress in Physics* **71**, 056501 (2008).

[6] R. O'HANDLEY, *Modern Magnetic Materials: Principles and Applications*, John Wiley & Sons Inc., 2000.

[7] J. A. OSBORN, *Physical Review* **67**, 351 (1945).

[8] J. DUBOWIK, *Physical Review B* **54**, 1088 (1996).

[9] M. GRIMSDITCH, Y. JACCARD, and I. K. SCHULLER, *Physical Review B* **58**, 11539 (1998).

[10] M. DARBY and E. ISAAC, *IEEE Transactions on Magnetics* **10**, 259 (1974).

[11] R. C. HALL, *Journal of Applied Physics* **30**, 816 (1959).

[12] C. KITTEL, *Physical Review Letters* **3**, 169 (1959).

[13] D.-S. WANG, R. WU, and A. J. FREEMAN, *Physical Review B* **47**, 14932 (1993).

[14] E. CALLEN, *Journal of Applied Physics* **39**, 519 (1968).

[15] E. CALLEN and H. B. CALLEN, *Physical Review* **139**, A455 (1965).

[16] R. C. O'HANDLEY, *Physical Review B* **18**, 930 (1978).

[17] C. ROBINSON, M. SAMANT, and E. MARINERO, *Applied Physics A* **49**, 619 (1989).

[18] X. YAN, M. HIRSCHER, T. EGAMI, and E. E. MARINERO, *Physical Review B* **43**, 9300 (1991).

[19] V. G. HARRIS, K. D. AYLESWORTH, B. N. DAS, W. T. ELAM, and N. C. KOON, *Physical Review Letters* **69**, 1939 (1992).

[20] J. FURTHMULLER, M. FAHNLE, and G. HERZER, *Journal of Physics F: Metal Physics* **16**, L255 (1986).

[21] M. FÄHNLE and T. EGAMI, *Journal of Applied Physics* **53**, 2319 (1982).

[22] D. SANDER, *Reports on Progress in Physics* **62**, 809 (1999).

[23] J. P. JAKUBOVICS, *Philosophical Magazine Part B* **38**, 401 (1978).

[24] B. D. CULLITY and C. D. GRAHAM, *Introduntion to Magnetic Materials, Second Edition*, John Wiley & Sons Inc., 2009.

[25] A. HUBERT and R. SCHÄFER, *Magnetic Domains: The Analytics of Magnetic Microstructures*, Springer, New York, 1998.

[26] C. KITTEL, *Reviews of Modern Physics* **21**, 541 (1949).

[27] S. S. P. PARKIN, M. HAYASHI, and L. THOMAS, *Science* **320**, 190 (2008).

[28] L. K. BOGART, D. ATKINSON, K. O'SHEA, D. MCGROUTHER, and S. MCVITIE, *Physical Review B* **79**, 054414 (2009).

[29] D. I. PAUL, *Journal of Applied Physics* **53**, 1649 (1982).

[30] V. H. SCHMIDT, *Ferroelectrics* **72**, 157 (1987).

[31] R. E. COHEN, *Nature* **358**, 136 (1992).

[32] R. COHEN, *Journal of Physics and Chemistry of Solids* **61**, 139 (2000).

[33] C. KITTEL, *Introduction to Solid State Physics*, John Wiley & Sons Inc., 2005.

[34] A. VON HIPPEL, *Reviews of Modern Physics* **22**, 221 (1950).

[35] H. D. MEGAW, *Proceedings of the Royal Society of London. Series A. Mathematical and Physical Sciences* **189**, 261 (1947).

[36] G. H. KWEI, A. C. LAWSON, S. J. L. BILLINGE, and S. W. CHEONG, *The Journal of Physical Chemistry* **97**, 2368 (1993).

[37] G. SHIRANE, H. DANNER, and R. PEPINSKY, *Physical Review* **105**, 856 (1957).

[38] S. K. STREIFFER, J. A. EASTMAN, D. D. FONG, C. THOMPSON, A. MUNKHOLM, M. V. RAMANA MURTY, O. AUCIELLO, G. R. BAI, and G. B. STEPHENSON, *Physical Review Letters* **89**, 067601 (2002).

[39] N. A. PERTSEV and A. G. ZEMBILGOTOV, *Journal of Applied Physics* **78**, 6170 (1995).

[40] S. PÖYKKÖ and D. J. CHADI, *Applied Physics Letters* **75**, 2830 (1999).

[41] B. MEYER and D. VANDERBILT, *Physical Review B* **65**, 104111 (2002).

[42] P. MARTON, I. RYCHETSKY, and J. HLINKA, *Physical Review B* **81**, 144125 (2010).

[43] X. ZHANG, T. HASHIMOTO, and D. C. JOY, *Applied Physics Letters* **60**, 784 (1992).

[44] J. HLINKA and P. MÁRTON, *Physical Review B* **74**, 104104 (2006).

[45] Q. Z. W. A. Goddard and III, *Applied Physics Letters* **89**, 182903 (2006).

[46] M. Fiebig, *Journal of Physics D: Applied Physics* **38**, R123 (2005).

[47] W. Eerenstein, N. D. Mathur, and J. F. Scott, *Nature* **442**, 759 (2006).

[48] R. Ramesh and N. A. Spaldin, *Nature Materials* **6**, 21 (2007).

[49] C.-W. Nan, M. I. Bichurin, S. Dong, D. Viehland, and G. Srinivasan, *Journal of Applied Physics* **103**, 031101 (2008).

[50] M. Bibes and A. Barthelemy, *Nature Materials* **7**, 425 (2008).

[51] J. Ma, J. Hu, Z. Li, and C.-W. Nan, *Advanced Materials* **23**, 1062 (2011).

[52] C. A. F. Vaz, *Journal of Physics: Condensed Matter* **24**, 333201 (2012).

[53] J. Wang, J. B. Neaton, H. Zheng, V. Nagarajan, S. B. Ogale, B. Liu, D. Viehland, V. Vaithyanathan, D. G. Schlom, U. V. Waghmare, N. A. Spaldin, K. M. Rabe, M. Wuttig, and R. Ramesh, *Science* **299**, 1719 (2003).

[54] J. Dho, X. Qi, H. Kim, J. L. MacManus-Driscoll, and M. G. Blamire, *Advanced Materials* **18**, 1445 (2006).

[55] C. Ederer and N. A. Spaldin, *Physical Review B* **71**, 060401 (2005).

[56] J. B. Neaton, C. Ederer, U. V. Waghmare, N. A. Spaldin, and K. M. Rabe, *Physical Review B* **71**, 014113 (2005).

[57] H. Bá, M. Bibes, A. Barthélémy, K. Bouzehouane, E. Jacquet, A. Khodan, J.-P. Contour, S. Fusil, F. Wyczisk, A. Forget, D. Lebeugle, D. Colson, and M. Viret, *Applied Physics Letters* **87**, 072508 (2005).

[58] T. Zhao, A. Scholl, F. Zavaliche, K. Lee, M. Barry, A. Doran, M. P. Cruz, Y. H. Chu, C. Ederer, N. A. Spaldin, R. R. Das, D. M. Kim, S. H. Baek, C. B. Eom, and R. Ramesh, *Nature Materials* **5**, 823 (2006).

[59] T. Kimura, T. Goto, H. Shintani, K. Ishizaka, T. Arima, and Y. Tokura, *Nature* **426**, 55 (2003).

[60] N. Hur, S. Park, P. A. Sharma, J. S. Ahn, S. Guha, and S.-W. Cheong, *Nature* **429**, 392 (2004).

[61] Y. Tokura and S. Seki, *Advanced Materials* **22**, 1554 (2010).

[62] H. Zheng, J. Wang, S. E. Lofland, Z. Ma, L. Mohaddes-Ardabili, T. Zhao, L. Salamanca-Riba, S. R. Shinde, S. B. Ogale, F. Bai, D. Viehland, Y. Jia, D. G. Schlom, M. Wuttig, A. Roytburd, and R. Ramesh, *Science* **303**, 661 (2004).

[63] J. Li, I. Levin, J. Slutsker, V. Provenzano, P. K. Schenck, R. Ramesh, J. Ouyang, and A. L. Roytburd, *Applied Physics Letters* **87**, 072909 (2005).

[64] F. Zavaliche, H. Zheng, L. Mohaddes-Ardabili, S. Y. Yang, Q. Zhan, P. Shafer, E. Reilly, R. Chopdekar, Y. Jia, P. Wright, D. G. Schlom, Y. Suzuki, and R. Ramesh, *Nano Letters* **5**, 1793 (2005).

[65] I. Levin, J. Li, J. Slutsker, and A. Roytburd, *Advanced Materials* **18**, 2044 (2006).

[66] H. Zheng, F. Straub, Q. Zhan, P.-L. Yang, W.-K. Hsieh, F. Zavaliche, Y.-H. Chu, U. Dahmen, and R. Ramesh, *Advanced Materials* **18**, 2747 (2006).

[67] Q. Zhan, R. Yu, S. P. Crane, H. Zheng, C. Kisielowski, and R. Ramesh, *Applied Physics Letters* **89**, 172902 (2006).

[68] J. Slutsker, I. Levin, J. Li, A. Artemev, and A. L. Roytburd, *Physical Review B* **73**, 184127 (2006).

[69] N. Dix, R. Muralidharan, J. Guyonnet, B. Warot-Fonrose, M. Varela, P. Paruch, F. Sánchez, and J. Fontcuberta, *Applied Physics Letters* **95**, 062907 (2009).

[70] E. Weal, S. Patnaik, Z. Bi, H. Wang, T. Fix, A. Kursumovic, and J. L. M. Driscoll, *Applied Physics Letters* **97**, 153121 (2010).

[71] N. M. Aimon, D. Hun Kim, H. Kyoon Choi, and C. A. Ross, *Applied Physics Letters* **100**, 092901 (2012).

[72] C.-G. Duan, S. S. Jaswal, and E. Y. Tsymbal, *Physical Review Letters* **97**, 047201 (2006).

[73] M. Weisheit, S. Fähler, A. Marty, Y. Souche, C. Poinsignon, and D. Givord, *Science* **315**, 349 (2007).

[74] M. Fechner, I. V. Maznichenko, S. Ostanin, A. Ernst, J. Henk, P. Bruno, and I. Mertig, *Physical Review B* **78**, 212406 (2008).

[75] M. K. Niranjan, J. P. Velev, C.-G. Duan, S. S. Jaswal, and E. Y. Tsymbal, *Physical Review B* **78**, 104405 (2008).

[76] C.-G. Duan, J. P. Velev, R. F. Sabirianov, Z. Zhu, J. Chu, S. S. Jaswal, and E. Y. Tsymbal, *Physical Review Letters* **101**, 137201 (2008).

[77] K. Nakamura, R. Shimabukuro, Y. Fujiwara, T. Akiyama, T. Ito, and A. J. Freeman, *Physical Review Letters* **102**, 187201 (2009).

[78] X. Hong, A. Posadas, A. Lin, and C. H. Ahn, *Physical Review B* **68**, 134415 (2003).

[79] T. Kanki, H. Tanaka, and T. Kawai, *Applied Physics Letters* **89**, 242506 (2006).

[80] H. Ohno, D. Chiba, F. Matsukura, T. Omiya, E. Abe, T. Dietl, Y. Ohno, and K. Ohtani, *Nature* **408**, 944 (2000).

[81] Y. D. Park, A. T. Hanbicki, S. C. Erwin, C. S. Hellberg, J. M. Sullivan, J. E. Mattson, T. F. Ambrose, A. Wilson, G. Spanos, and B. T. Jonker, *Science* **295**, 651 (2002).

[82] D. Chiba, M. Yamanouchi, F. Matsukura, and H. Ohno, *Science* **301**, 943 (2003).

[83] I. Stolichnov, S. W. E. Riester, H. J. Trodahl, N. Setter, A. W. Rushforth, K. W. Edmonds, R. P. Campion, C. T. Foxon, B. L. Gallagher, and T. Jungwirth, *Nature Materials* **7**, 464 (2008).

[84] D. Chiba, M. Sawicki, Y. Nishitani, Y. Nakatani, F. Matsukura, and H. Ohno, *Nature* **455**, 515 (2008).

[85] K. Yamauchi, B. Sanyal, and S. Picozzi, *Applied Physics Letters* **91**, 062506 (2007).

[86] V. Garcia, M. Bibes, L. Bocher, S. Valencia, F. Kronast, A. Crassous, X. Moya, S. Enouz-Vedrenne, A. Gloter, D. Imhoff, C. Deranlot, N. D. Mathur, S. Fusil, K. Bouzehouane, and A. Barthélémy, *Science* **327**, 1106 (2010).

[87] D. Pantel, S. Goetze, D. Hesse, and M. Alexe, *Nature Materials* **11**, 289 (2012).

[88] L. Bocher, A. Gloter, A. Crassous, V. Garcia, K. March, A. Zobelli, S. Valencia, S. Enouz-Vedrenne, X. Moya, N. D. Marthur, C. Deranlot, S. Fusil, K. Bouzehouane, M. Bibes, A. Barthélémy, C. Colliex, and O. Stéphan, *Nano Letters* **12**, 376 (2012).

[89] L. W. Martin, Y.-H. Chu, M. B. Holcomb, M. Huijben, P. Yu, S.-J. Han, D. Lee, S. X. Wang, and R. Ramesh, *Nano Letters* **8**, 2050 (2008), PMID: 18547121.

[90] V. Laukhin, V. Skumryev, X. Martí, D. Hrabovsky, F. Sánchez, M. V. García-Cuenca, C. Ferrater, M. Varela, U. Lüders, J. F. Bobo, and J. Fontcuberta, *Physical Review Letters* **97**, 227201 (2006).

[91] V. Skumryev, V. Laukhin, I. Fina, X. Martí, F. Sánchez, M. Gospodinov, and J. Fontcuberta, *Physical Review Letters* **106**, 057206 (2011).

[92] Y.-H. Chu, L. W. Martin, M. B. Holcomb, M. Gajek, S.-J. Han, Q. He, N. Balke, C.-H. Yang, D. Lee, W. Hu, Q. Zhan, P.-L. Yang, A. Fraile-Rodriguez, A. Scholl, S. X. Wang, and R. Ramesh, *Nature Materials* **7**, 478 (2008).

[93] H. Béa, M. Bibes, F. Ott, B. Dupé, X.-H. Zhu, S. Petit, S. Fusil, C. Deranlot, K. Bouzehouane, and A. Barthélémy, *Physical Review Letters* **100**, 017204 (2008).

[94] D. Lebeugle, A. Mougin, M. Viret, D. Colson, and L. Ranno, *Physical Review Letters* **103**, 257601 (2009).

[95] S. M. Wu, S. A. Cybart, P. Yu, M. D. Rossell, J. X. Zhang, R. Ramesh, and R. C. Dynes, *Nature Materials* **9**, 756 (2010).

[96] D. Lebeugle, A. Mougin, M. Viret, D. Colson, J. Allibe, H. Béa, E. Jacquet, C. Deranlot, M. Bibes, and A. Barthélémy, *Physical Review B* **81**, 134411 (2010).

[97] J. T. Heron, M. Trassin, K. Ashraf, M. Gajek, Q. He, S. Y. Yang, D. E. Nikonov, Y.-H. Chu, S. Salahuddin, and R. Ramesh, *Physical Review Letters* **107**, 217202 (2011).

[98] C. Thiele, K. Dörr, O. Bilani, J. Rödel, and L. Schultz, *Physical Review B* **75**, 054408 (2007).

[99] C. Thiele, K. Dörr, S. Fähler, L. Schultz, D. C. Meyer, A. A. Levin, and P. Paufler, *Applied Physics Letters* **87**, 262502 (2005).

[100] J.-Y. Kim, L. Yao, and S. van Dijken, *Journal of Physics: Condensed Matter* **25**, 082205 (2013).

[101] Z. G. Sheng, J. Gao, and Y. P. Sun, *Physical Review B* **79**, 174437 (2009).

[102] J. J. Yang, Y. G. Zhao, H. F. Tian, L. B. Luo, H. Y. Zhang, Y. J. He, and H. S. Luo, *Applied Physics Letters* **94**, 212504 (2009).

[103] J. H. Park, J.-H. Lee, M. G. Kim, Y. K. Jeong, M.-A. Oak, H. M. Jang, H. J. Choi, and J. F. Scott, *Physical Review B* **81**, 134401 (2010).

[104] J. H. Park, Y. K. Jeong, S. Ryu, J. Y. Son, and H. M. Jang, *Applied Physics Letters* **96**, 192504 (2010).

[105] Y. Yang, Z. L. Luo, H. Huang, Y. Gao, J. Bao, X. G. Li, S. Zhang, Y. G. Zhao, X. Chen, G. Pan, and C. Gao, *Applied Physics Letters* **98**, 153509 (2011).

[106] M. Liu, O. Obi, J. Lou, Y. Chen, Z. Cai, S. Stoute, M. Espanol, M. Lew, X. Situ, K. S. Ziemer, V. G. Harris, and N. X. Sun, *Advanced Functional Materials* **19**, 1826 (2009).

[107] J.-H. Kim, K.-S. Ryu, J.-W. Jeong, and S.-C. Shin, *Applied Physics Letters* **97**, 252508 (2010).

[108] T. Wu, A. Bur, K. Wong, P. Zhao, C. S. Lynch, P. K. Amiri, K. L. Wang, and G. P. Carman, *Applied Physics Letters* **98**, 262504 (2011).

[109] C.-J. Hsu, J. L. Hockel, and G. P. Carman, *Applied Physics Letters* **100**, 092902 (2012).

[110] R. K. Zheng, Y. Wang, H. L. W. Chan, C. L. Choy, and H. S. Luo, *Physical Review B* **75**, 212102 (2007).

[111] J. Wang, F. X. Hu, R. W. Li, J. R. Sun, and B. G. Shen, *Applied Physics Letters* **96**, 052501 (2010).

[112] A. D. Rata, A. Herklotz, K. Nenkov, L. Schultz, and K. Dörr, *Physical Review Letters* **100**, 076401 (2008).

[113] R. K. Zheng, Y. Jiang, Y. Wang, H. L. W. Chan, C. L. Choy, and H. S. Luo, *Physical Review B* **79**, 174420 (2009).

[114] Y. K. Fetisov and G. Srinivasan, *Applied Physics Letters* **93**, 033508 (2008).

[115] Y. Chen, J. Wang, M. Liu, J. Lou, N. X. Sun, C. Vittoria, and V. G. Harris, *Applied Physics Letters* **93**, 112502 (2008).

[116] J. Das, M. Li, S. S. Kalarickal, S. Altmannshofer, K. S. Buchanan, J. F. Li, and D. Viehland, *Applied Physics Letters* **96**, 222508 (2010).

[117] J. F. Scott, *Advanced Materials* **22**, 5315 (2010).

[118] M. Liu, J. Lou, S. Li, and N. X. Sun, *Advanced Functional Materials* **21**, 2593 (2011).

[119] N. Tiercelin, Y. Dusch, A. Klimov, S. Giordano, V. Preobrazhensky, and P. Pernod, *Applied Physics Letters* **99**, 192507 (2011).

[120] D. E. Parkes, S. A. Cavill, A. T. Hindmarch, P. Wadley, F. McGee, C. R. Staddon, K. W. Edmonds, R. P. Campion, B. L. Gallagher, and A. W. Rushforth, *Applied Physics Letters* **101**, 072402 (2012).

[121] J.-M. Hu, Z. Li, L.-Q. Chen, and C.-W. Nan, *Nature Communications* **2** (2011).

[122] J.-M. Hu, Z. Li, L.-Q. Chen, and C.-W. Nan, *Advanced Materials* **24**, 2869 (2012).

[123] A. Brandlmaier, S. Geprägs, G. Woltersdorf, R. Gross, and S. T. B. Goennenwein, *Journal of Applied Physics* **110**, 043913 (2011).

[124] M. K. Lee, T. K. Nath, C. B. Eom, M. C. Smoak, and F. Tsui, *Applied Physics Letters* **77**, 3547 (2000).

[125] W. Eerenstein, M. Wiora, J. L. Prieto, J. F. Scott, and N. D. Mathur, *Nature Materials* **6**, 348 (2007).

[126] H. F. Tian, T. L. Qu, L. B. Luo, J. J. Yang, S. M. Guo, H. Y. Zhang, Y. G. Zhao, and J. Q. Li, *Applied Physics Letters* **92**, 063507 (2008).

[127] C. A. F. Vaz, J. Hoffman, A.-B. Posadas, and C. H. Ahn, *Applied Physics Letters* **94**, 022504 (2009).

[128] G. E. Sterbinsky, B. W. Wessels, J.-W. Kim, E. Karapetrova, P. J. Ryan, and D. J. Keavney, *Applied Physics Letters* **96**, 092510 (2010).

[129] S. Sahoo, S. Polisetty, C.-G. Duan, S. S. Jaswal, E. Y. Tsymbal, and C. Binek, *Physical Review B* **76**, 092108 (2007).

[130] T. Taniyama, K. Akasaka, D. Fu, and M. Itoh, *Journal of Applied Physics* **105**, 07D901 (2009).

[131] S. Brivio, D. Petti, R. Bertacco, and J. C. Cezar, *Applied Physics Letters* **98**, 092505 (2011).

[132] Y. Shirahata, T. Nozaki, G. Venkataiah, H. Taniguchi, M. Itoh, and T. Taniyama, *Applied Physics Letters* **99**, 022501 (2011).

[133] G. Venkataiah, Y. Shirahata, M. Itoh, and T. Taniyama, *Applied Physics Letters* **99**, 102506 (2011).

[134] G. Venkataiah, Y. Shirahata, I. Suzuki, M. Itoh, and T. Taniyama, *Journal of Applied Physics* **111**, 033921 (2012).

[135] F. D. Czeschka, S. Geprägs, M. Opel, S. T. B. Goennenwein, and R. Gross, *Applied Physics Letters* **95**, 062508 (2009).

[136] T. Brintlinger, S.-H. Lim, K. H. Baloch, P. Alexander, Y. Qi, J. Barry, J. Melngailis, L. Salamanca-Riba, I. Takeuchi, and J. Cumings, *Nano Letters* **10**, 1219 (2010).

[137] S. Geprägs, A. Brandlmaier, M. Opel, R. Gross, and S. T. B. Goennenwein, *Applied Physics Letters* **96**, 142509 (2010).

[138] A. T. Hindmarch, C. J. Kinane, M. MacKenzie, J. N. Chapman, M. Henini, D. Taylor, D. A. Arena, J. Dvorak, B. J. Hickey, and C. H. Marrows, *Physical Review Letters* **100**, 117201 (2008).

[139] R. C. Hall, *Journal of Applied Physics* **31**, S157 (1960).

[140] D. E. Wolfe and J. Singh, *Surface and Coatings Technology* **124**, 142 (2000).

[141] C. HENRY, *Analytical Chemistry* **68**, 625A (1996).

[142] J. L. VOSSEN and W. KERN, *Thin film processes. 2*, Gulf Professional Publishing, 1991.

[143] J. J. KREBS, B. T. JONKER, and G. A. PRINZ, *Journal of Applied Physics* **61**, 2596 (1987).

[144] M. D. JOHNSON, C. ORME, A. W. HUNT, D. GRAFF, J. SUDIJONO, L. M. SANDER, and B. G. ORR, *Physical Review Letters* **72**, 116 (1994).

[145] T. TANIYAMA, K. AKASAKA, D. FU, M. ITOH, H. TAKASHIMA, and B. PRIJAMBOEDI, *Journal of Applied Physics* **101**, 09F512 (2007).

[146] R. K. WAITS, *Journal of Vacuum Science and Technology* **15**, 179 (1978).

[147] I. SAFI, *Surface and Coatings Technology* **127**, 203 (2000).

[148] J. MUSIL, P. BAROCH, J. VLCEK, K. NAM, and J. HAN, *Thin Solid Films* **475**, 208 (2005).

[149] P. KELLY and R. ARNELL, *Vacuum* **56**, 159 (2000).

[150] S. YUASA, Y. SUZUKI, T. KATAYAMA, and K. ANDO, *Applied Physics Letters* **87**, 242503 (2005).

[151] M. FREISER, *IEEE Transactions on Magnetics* **4**, 152 (1968).

[152] Z. Q. QIU and S. D. BADER, *Review of Scientific Instruments* **71**, 1243 (2000).

[153] M. J. DONAHUE and D. G. PORTER, OOMMF User's Guide, Version 1.0, Technical report, Interagency Report NISTIR 6376, 1999.

[154] W. WANG, C. MU, B. ZHANG, Q. LIU, J. WANG, and D. XUE, *Computational Materials Science* **49**, 84 (2010).

[155] V. VAS"KO, J. RANTSCHLER, and M. KIEF, *IEEE Transactions on Magnetics* **40**, 2335 (2004).

[156] S. W. SUN and R. C. O'HANDLEY, *Physical Review Letters* **66**, 2798 (1991).

[157] G. BOCHI, O. SONG, and R. C. O'HANDLEY, *Physical Review B* **50**, 2043 (1994).

Historically used for navigation; currently utilized in data storage, actuators and sensors—magnetic devices are an indispensible part of our daily lives. However, current magnetic technologies are too complex to incorporate into electronics as components continue to miniaturize. Using an electric field to control magnetism could lead to a new generation of simple, low power magnetic devices. This thesis focuses on domain coupling in multiferroic heterostructures, a group of hybrid materials that couple electric-field-sensitive ferroelectric materials and magnetic-field-sensitive ferromagnetic materials. As a key result, electric field controlled local magnetization rotation and magnetic domain wall motion are demonstrated.

Aalto-DD 106/2013

ISBN 978-952-60-5230-4
ISBN 978-952-60-5231-1 (pdf)
ISSN-L 1799-4934
ISSN 1799-4934
ISSN 1799-4942 (pdf)

Aalto University
School of Science
Department of Applied Physics
www.aalto.fi